Nano-Micro Letters

e-ISSN 2150-5551
CN 31-2103/TB

ARTICLE

https://doi.org/10.1007/s40820-025-01915-w

Cite as
Nano-Micro Lett.
(2026) 18:90

Received: 18 May 2025
Accepted: 13 August 2025
© The Author(s) 2025

Multiscale Theoretical Calculations Empower Robust Electric Double Layer Toward Highly Reversible Zinc Anode

Yufan Xia[1], Zhen Luo[1], Shuang Chen[1], Yang Xiang[1], Gao Weng[1], Hongge Pan[1,3], Ben Bin Xu[4], Mi Yan[1], Yinzhu Jiang[1,2] ✉

HIGHLIGHTS

- A multiscale theoretical framework deciphers the molecular-ionic dynamics of the electric double layer (EDL) in aqueous rechargeable zinc batteries, correlating interfacial water aggregation, anion-specific adsorption, and electric field inhomogeneity to parasitic reactions and dendrite growth, thereby establishing EDL-driven design principles for ultra-stable Zn anodes.
- Molecular adsorption engineering creates a localized "water-poor and anion-expelled" EDL configuration that suppresses hydrogen evolution and by-product formation while enabling dense Zn electrodeposition through flattened interfacial potential gradients and reduced Zn^{2+} electrostatic repulsion.

ABSTRACT The electric double layer (EDL) at the electrochemical interface is crucial for ion transport, charge transfer, and surface reactions in aqueous rechargeable zinc batteries (ARZBs). However, Zn anodes routinely encounter persistent dendrite growth and parasitic reactions, driven by the inhomogeneous charge distribution and water-dominated environment within the EDL. Compounding this, classical EDL theory, rooted in mean-field approximations, further fails to resolve molecular-scale interfacial dynamics under battery-operating conditions, limiting mechanistic insights. Herein, we established a multiscale theoretical calculation framework from single molecular characteristics to interfacial ion distribution, revealing the EDL's structure and interactions between different ions and molecules, which helps us understand the parasitic processes in depth. Simulations demonstrate that water dipole and sulfate ion adsorption at the inner Helmholtz plane drives severe hydrogen evolution and by-product formation. Guided by these insights, we engineered a "water-poor and anion-expelled" EDL using 4,1',6'-trichlorogalactosucrose (TGS) as an electrolyte additive. As a result, Zn||Zn symmetric cells with TGS exhibited stable cycling for over 4700 h under a current density of 1 mA cm^{-2}, while $NaV_3O_8 \cdot 1.5H_2O$-based full cells kept 90.4% of the initial specific capacity after 800 cycles at 5 A g^{-1}. This work highlights the power of multiscale theoretical frameworks to unravel EDL complexities and guide high-performance ARZB design through integrated theory-experiment approaches.

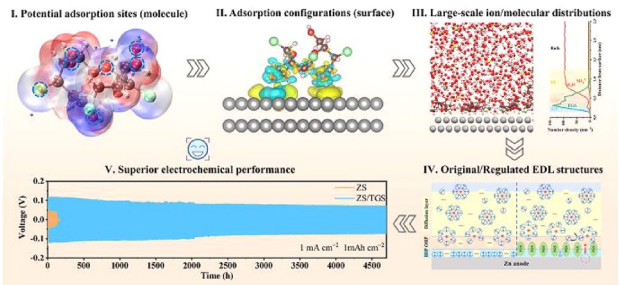

KEYWORDS Zn anode; Theoretical calculations; Electric double layers; Aqueous rechargeable zinc batteries

Yufan Xia and Zhen Luo have contributed equally to this work.

✉ Yinzhu Jiang, yzjiang@zju.edu.cn
[1] School of Materials Science and Engineering, Zhejiang University, Hangzhou 310027, People's Republic of China
[2] Future Science Research Institute, ZJU-Hangzhou Global Scientific and Technological Innovation Center, Zhejiang University, Hangzhou 311215, People's Republic of China
[3] Institute of Science and Technology for New Energy, Xi'an Technological University, Xi'an 710021, People's Republic of China
[4] Mechanical and Construction Engineering, Faculty of Engineering and Environment, Northumbria University, Newcastle Upon Tyne NE1 8ST, UK

Published online: 25 December 2025

1 Introduction

Electrochemical reaction processes, dynamically occurring at electrochemical interfaces, are the cornerstone of energy storage and conversion systems, dictating the performance and stability of devices such as batteries, supercapacitors, and fuel cells [1–3]. Due to the inner electric field between the anode and the cathode, or the difference in the equilibrium state between the electrode and the bulk electrolyte, a rearrangement of the solvated ions, solvent molecules, and adsorbed species takes place on the electrode surface, which leads to the formation of an electrochemical potential difference from the surface to the bulk electrolyte [4, 5]. Under this potential difference, an electric double layer (EDL) forms at the interface between the electrode and the liquid electrolyte, representing one of the most fundamental and critical concepts in electrochemistry [6]. Most importantly, the properties of the EDL directly govern the electrochemical reaction processes at the electrode-electrolyte interfaces, thereby influencing the electrochemical responses and performances of practical devices [7, 8].

The understanding of the EDL structure dates back to the early nineteenth century [9], beginning with Helmholtz's pioneering work in 1879 (Fig. S1). Building on Helmholtz's foundational contributions, researchers made significant advancements, culminating in the well-known Gouy-Chapman-Stern (GCS) model [10]. This model divides the EDL into two layers: (1) the Stern layer (or Helmholtz plane, HP), which interacts directly with the electrode surface, and (2) the Gouy–Chapman layer (or diffuse layer, DL), which extends into the bulk electrolyte. Despite its widespread use in studying electrode-electrolyte interfaces [11–14], the GCS model fails to account for the specific adsorption of water molecules and anions, leading to inaccuracies in describing the detailed distribution of ions and solvents at the interface. To address these limitations, further electrochemical studies were conducted by Grahame [15] and Bockris et al. [16], ultimately resulting in the detailed Bockris-Devanathan-Müller (BDM) model. The BDM model refines the HP by dividing it into an inner Helmholtz plane (IHP) and an outer Helmholtz plane (OHP). It reveals that water molecules near the electrode surface orient directionally due to their dipole interactions with the surface. As a result, the IHP becomes a complex mixture of specifically adsorbed ions and oriented water molecules, while the OHP is populated primarily by solvated ions. This insight into the structured arrangement of water and ions at the interface has profoundly deepened our understanding of interfacial phenomena in electrochemical systems.

Aqueous rechargeable zinc batteries (ARZBs), due to their low cost, high safety, and environmental compatibility, have emerged as one of the most attractive alternatives for large-scale energy storage [17–19]. However, the Zn metal anode is confronted with issues such as rampant dendrite growth and severe parasitic reactions, which occur at the anode–electrolyte interface (AEI) and result in low Coulombic efficiency (CE) during the Zn plating/stripping process [20–22]. As reported by previous research [23], the EDL structure plays a decisive role in governing ion transport, charge distribution, and Zn deposition at AEI. On the one hand, the specific adsorption of ions and water molecules within IHP induces inhomogeneous charge distribution on the Zn anode surface, which guides Zn^{2+} diffusion to the prior nucleation sites and promotes the uneven Zn deposition with dendritic morphology [24, 25]. On the other hand, the solvating water in the Zn^{2+} shell would migrate from the bulk electrolyte to the EDL and be pulled across the IHP, which has a higher reduction potential than free water due to the positive charge in the cation, making the hydrogen more reactive [26, 27]. Consequently, these water molecules would be decomposed to release H_2 along with the reduction of Zn^{2+}, which is known as the hydrogen evolution reaction (HER). Despite the critical role of EDL in stabilizing the Zn anode, investigating the EDL at AEI notoriously remains challenging due to the limitations of classical mean-field descriptions for the classical EDL models [4, 5, 28, 29]. Therefore, there is a pressing need to address key unsolved questions: What are the specific molecular and ion distributions within the EDL? Are anions specifically adsorbed, and if so, in which layer? How can the EDL structure be adjusted in scenarios where side reactions dominate? To address these complexities, multiscale simulations, particularly those focusing on interfacial dynamics and ion-specific interactions [30], offer a powerful approach to bridging the gap between classical theory and experimental observations.

In this study, we present an innovative approach to investigating EDL by employing a multiscale simulation platform that integrates quantum chemistry (QC), density functional theory (DFT), and classical molecular dynamics (CMD), further validated by characterization techniques and battery performance (Fig. 1). In detail, the potential adsorption sites

© The authors
https://doi.org/10.1007/s40820-025-01915-w

for molecules on the Zn metal surface could be identified by QC calculations. Subsequently, DFT-based surface adsorption calculations are performed to characterize adsorption states, including specific adsorption sites, orientations, charge density, and corresponding adsorption energies, which provide insights into the preferential adsorption of certain molecules. Finally, CMD simulations are employed to reveal the dynamic processes of EDL formation and to model the molecular/ionic distributions near the AEI, offering a deeper understanding of the surface hydrogen bond (H-bond) network. Our integrated multiscale simulation platform provides a unique and comprehensive framework for interpreting EDL behavior, equipping researchers with valuable insights for efficient modification of EDL structure toward a robust Zn anode.

In virtue of this multiscale calculation framework, the EDL structure in typical zinc sulfate ($ZnSO_4$) aqueous electrolytes is characterized as follows: the IHP consists of orderly adsorbed water dipoles and SO_4^{2-} anions, which are tightly bound to the Zn metal surface. In contrast, the OHP is predominantly occupied by hydrated complexes, such as $Zn^{2+}(H_2O)_6$ or $Zn^{2+}(H_2O)_5SO_4^{2-}$, which are more loosely associated with the surface. Beyond the HP, the DL contains ions in equilibrium with the bulk electrolyte, contributing to the overall ionic concentration near the electrode interface. The molecular and ionic distributions revealed by these simulations align with the predictions of the classical BDM model. However, the presence of abundant free water molecules and SO_4^{2-} anions within HP leads to undesirable parasitic reactions. These reactions accelerate the corrosion of the Zn anode and generate harmful hydroxide ions (OH^-) within the IHP [31, 32], resulting in the formation of insulating and uneven by-products, such as $Zn_4SO_4(OH)_6{\cdot}xH_2O$ (ZSH) [33]. Besides, the deteriorative surface condition further exacerbates the tip effect, resulting in uncontrollable Zn dendrite growth, which degrades the long-term stability of the Zn anode [25].

To construct a "water-poor and anion-expelled" EDL structure to stabilize the Zn anode, we investigate the effect of 4,1',6'-trichlorogalactosucrose (TGS), a promising and cost-effective electrolyte additive, as a case study. The modulation of the EDL structure is intricately influenced by both substrate architecture and electrolyte composition. Previous strategies based on substrate architecture engineering, primarily by modifying surface charge density [12, 34], have been proven to be effective in regulating the EDL structure and reshaping the interface-localized distribution of ions, thereby promoting uniform Zn deposition and suppressing parasitic reactions [35–37]. In contrast, electrolyte design, especially through the incorporation of functional additives, provides a more versatile, solution-processable, self-adaptive, and dynamic approach for modulating the EDL at the electrode-electrolyte interface [31, 38–40]. Our additive-based EDL engineering strategy distinguishes itself by enabling targeted regulation of interfacial ion distributions without altering the electrode structure, thereby achieving enhanced Zn reversibility via a readily facile approach. Specifically, TGS is introduced to regulate the distribution and chemical environment of H_2O and SO_4^{2-} within the HP. The simulation results reveal that TGS spontaneously adsorbs into the IHP of the EDL, disrupting the aggregation of H_2O molecules and creating a water-poor environment near the Zn surface. Simultaneously, the surface H-bond network is reconstructed due to the adsorption of TGS molecules. Additionally, SO_4^{2-} anions are expelled from the IHP and OHP, effectively suppressing the formation of ZHS. By modifying the EDL with TGS, the overpotential increases, and the critical nucleation size decreases, promoting uniform Zn deposition and reducing dendrite formation. The efficacy of the modified EDL structure with TGS additive, given by this multiscale simulation platform, is demonstrated by the enhanced Zn anode performance. Encouragingly, Zn||Cu asymmetric cells using TGS electrolyte additive achieved stable cycling for over 1100 cycles at a current density of 1 mA cm^{-2}, with an average CE of 99.49%. In parallel, Zn||Zn symmetric cells maintained a stable operation lifespan for over 4700 h at 1 mA cm^{-2}, significantly outperforming cells with conventional $ZnSO_4$ electrolytes. Moreover, full cells incorporating $NaV_3O_8{\cdot}1.5H_2O$ cathodes also exhibited superior performance with TGS, achieving a high capacity retention of 90.4% after 800 cycles at 5 A g^{-1}.

2 Computational Methods

2.1 Quantum Chemistry Calculations

Quantum chemistry calculations were conducted using the Gaussian 16 software package. Structural optimizations and frequency calculations for the electrostatic potential (ESP) were performed at the M06-2X/def2-TZVP level of theory [41, 42]. To accurately simulate the aqueous environment,

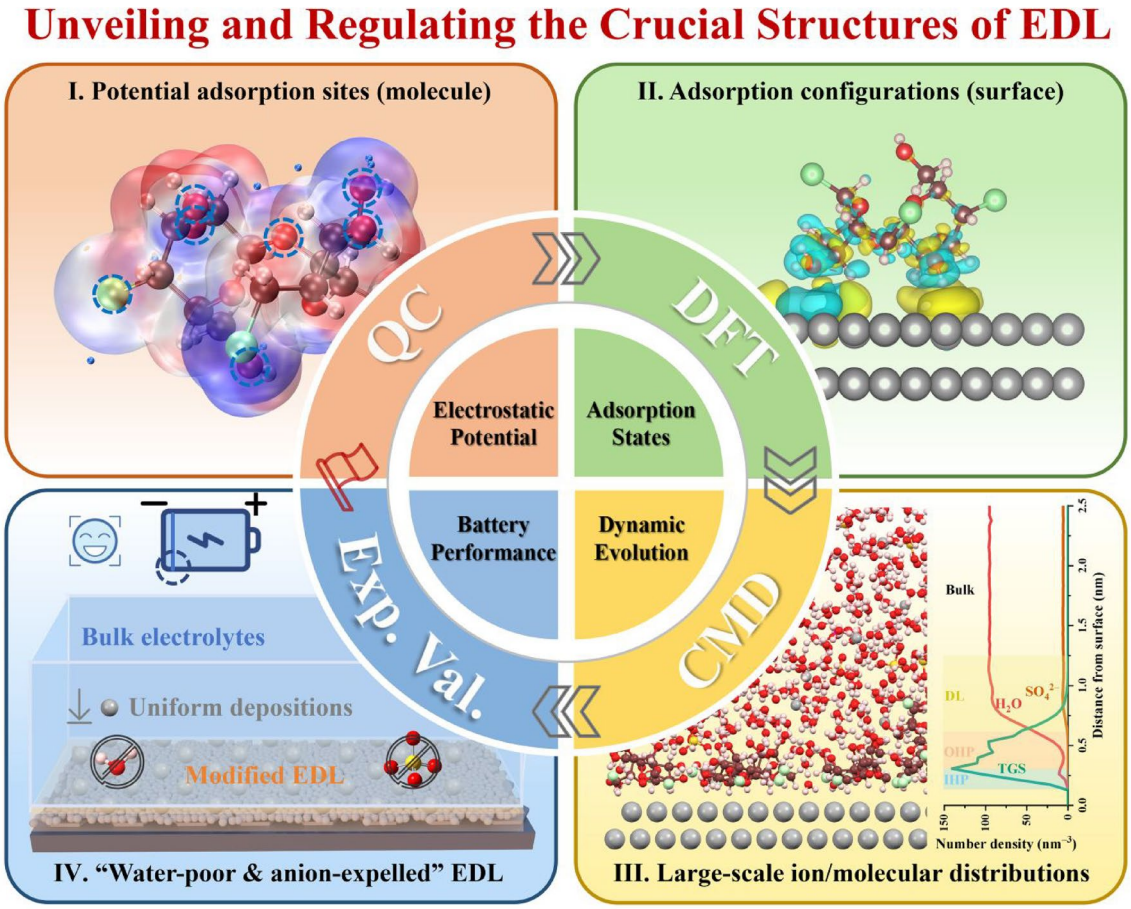

Fig. 1 Schematic illustration of an advanced multiscale theoretical calculations framework and experimental validations to reveal regulated EDL structures. Exp. Val. is an abbreviation for experimental validations

the universal solvation model based on density (SMD) was employed [43], ensuring a precise representation of solvation effects. The independent gradient model based on Hirshfeld (IGMH) [44] was employed to investigate the interactions between TGS and H_2O. This model provides an accurate framework for understanding interactions in chemical systems [44]. The molecular surface electrostatic potential was plotted using Multiwfn software [45, 46].

For solvation free energy calculations, geometry optimizations of the studied systems were executed using the M06-2X functional with the TZVP basis set. Subsequently, single-point energy calculations were performed at the M06-2X/def2-TZVPP level of theory. The solvation energy was derived from the single-point energy difference calculated using the M05-2X/6-31G* level of theory, both in the gas phase and within the SMD solvation model (using water as the solvent). Based on prior molecular dynamics and experimental studies, the coordination number of Zn^{2+} was constrained to six [47].

The free energy (G) of the solute in a solvent environment (at 298.15 K and 1 M concentration) was calculated using the following formula [48]:

$$G_{solvent} = G_{gas} + G_{solution} + 1.89\ \text{kcal mol}^{-1}$$

where G_{gas} represents the gas-phase free energy of the solute at 1 atm, $G_{solution}$ denotes the free energy of solvation calculated using the implicit solvent model, and 1.89 kcal mol^{-1} accounts for the free energy change from 1 atm to 1 M standard state conditions. The relative free energies (ΔG) for the Zn^{2+} solvates, referenced to $Zn^{2+}(H_2O)_6$, were defined as follows [48]:

$$\Delta G = G_{[Zn^{2+}(H_2O)_x(n)_{(6-x)}]} - G_{[Zn^{2+}(H_2O)_6]} + (6-x)G_{H_2O} - (6-x)G_n$$

© The authors
https://doi.org/10.1007/s40820-025-01915-w

where x represents the coordination number of Zn^{2+}, with $x = 5, 6$. This approach facilitates a comprehensive analysis of the solvation structures and energetics of Zn^{2+} across various solvation environments.

The binding energy (E_{bind}) is calculated using the following formula:

$$E_{bind} = E_{AB} - E_A - E_B - E_{BSSE}$$

where E_{AB}, E_A, and E_B represent the total energies of the AB complex, the isolated species A, and the isolated species B, respectively. E_{BSSE} denotes the basis set superposition error (BSSE) correction energy, which is applied using the counterpoise method [49].

2.2 Density Functional Theory Calculations

The Vienna Ab-initio Simulation Package (VASP) software [50, 51] was utilized to conduct adsorption and HER barrier calculations. The Perdew-Burke-Ernzerhof (PBE) functional within the generalized gradient approximation (GGA) was employed [52]. The projector augmented-wave (PAW) method was applied to accurately describe the interactions between core and valence electrons [53]. An energy cutoff of 500 eV was set, and a Γ-centered k-point mesh grid of $2 \times 2 \times 1$ was used for geometry optimization. Grimme's DFT-D3 method was also implemented to account for van der Waals (vdW) interactions [54].

The computational model consisted of a Zn (002) surface slab composed of four Zn atomic layers, with the bottom two layers fixed. A vacuum layer of 15 Å was included to avoid interactions between periodic images. Atomic positions were relaxed until the energy converged to less than 10^{-5} eV, and the maximum force on any atom was reduced to less than 0.02 eV $Å^{-1}$.

The adsorption energy ($E_{ads.}$) is calculated using the following equation:

$$E_{ads.} = E_{slab/adsorbate} - E_{slab} - E_{adsorbate}$$

where $E_{slab/adsorbate}$ is the total energy of the slab with the adsorbate, E_{slab} is the energy of the clean slab, and $E_{adsorbate}$ is the energy of the isolated adsorbate molecule.

The HER activity was investigated under acidic conditions, incorporating van der Waals interactions to provide an accurate description of the system. The Gibbs free energy change (ΔG_H), a critical parameter for characterizing HER activity, is determined using the following equation [55]:

$$\Delta G_H = \Delta E_H + \Delta E_{ZPE} - T\Delta S_H$$

where ΔE_H is the change in electronic energy, ΔE_{ZPE} is the change in zero-point energy, T is the temperature, and ΔS_H is the change in entropy. This comprehensive approach enables an accurate assessment of the adsorption properties and HER activity on the Zn (002) surface, providing valuable insights into the electrochemical behavior of the system.

2.3 Bulk Classical Molecular Dynamics

Classical molecular dynamics simulations were conducted using GROMACS 2022.2 [56]. The OPC3 water model was utilized to simulate water molecules [57], while the Merz force field was employed for Zn ions [58], as these models provide optimal accuracy for our system. The general Amber force field (GAFF) parameters [59] for sulfate ions and TGS molecules were generated using the Sobtop program, with atomic charges derived from restrained electrostatic potential (RESP2) calculations [60] performed by Multiwfn [46]. The simulation system consisted of 4440 water molecules, 160 Zn ions, 160 sulfate anions, and 40 TGS molecules. Atomic charges of all ions were multiplied by a scale factor of 0.7 to correct the polarization effect of ions.

The simulation protocol commenced with energy minimization using the steepest descent method to eliminate any unfavorable interactions. Following this, the system was gradually heated from 10 to 298.15 K over a period of 100 ps, followed by an additional 100 ps at the target temperature to ensure stabilization. Pre-equilibration was performed under isothermal-isobaric (NPT) conditions at 1 bar for 10 ns. The production run involved a 20 ns simulation under the canonical ensemble (NVT).

A time step of 1 fs was employed for all simulations. In the NPT simulations, temperature control was achieved using a V-rescale thermostat [61] with a time constant of 1 ps, while pressure was maintained with the Berendsen barostat [62] with a time constant of 3 ps. For the NVT simulations, a Nosé-Hoover thermostat [63, 64] with a time constant of 1 ps was used. Electrostatic interactions were calculated using the particle-mesh Ewald (PME) method [65, 66], with a cutoff distance of 1.2 nm. System visualization and analysis of ion association states were carried out using VMD software [67].

2.4 Interfacial Classical Molecular Dynamics

An interfacial model, illustrated in Fig. S23, was developed to investigate the EDL structures. This model comprises two Zn metal electrodes, an electrolyte containing an equivalent number of electrolyte species as those employed in bulk simulations, and a vacuum layer to replicate the interfacial environment.

The dimensions of the periodic simulation cells in the *x*- and *y*-directions are 55.12 Å × 55.69 Å for ZS electrolyte and 55.28 Å × 55.85 Å for ZS/TGS electrolyte, as recorded in Table S3. The electrolyte thickness separating the two Zn metal anodes is approximately 50.0 Å; specifically, for the ZS electrolyte, the thickness is 49.96 Å, while for the ZS/TGS electrolyte, it measures 53.64 Å. These values were obtained through equilibration simulations, with the detailed methodology illustrated in Fig. S22. The selected thickness is sufficiently substantial to ensure the manifestation of bulk electrolyte behavior in the central region of the simulation cell [68].

In these simulations, the Zn anodes were fixed in position, and the Lennard-Jones parameters for the Zn atoms were defined as $\sigma = 2.44$ Å and $\varepsilon = 3.022$ kJ mol^{-1}, which have been shown to provide accurate representations of the interfacial interactions [32]. In the subsequent calculations, the left Zn anode is assigned a positive charge, while the right anode is negatively charged, in accordance with considerations of the potential of zero charge (PZC).

For the force field parameters governing the molecules and ions (Zn^{2+}, SO_4^{2-}, H_2O, and TGS), the same parameters as those utilized in the bulk electrolyte simulations were employed to ensure consistency across the simulations. Following the pre-equilibration simulations of the bulk electrolyte, Zn (002)-electrolyte-Zn (002) structures were constructed. Energy minimizations were performed using the steepest descent method to optimize the system configuration. Subsequently, the system was subjected to a heating protocol, gradually increasing the temperature from 10 to 600 K over a period of approximately 100 ps. This was followed by an additional equilibration period of 100 ps at the target temperature. The relatively high temperature of 600 K was selected to facilitate the formation of uniform and saturated EDL structures within the constraints of the limited simulation time [69].

For the interface simulations, pre-equilibration was conducted under NPT conditions at a pressure of 1 bar for a duration of 10 ns. The production run consisted of a 20 ns simulation performed under the NVT, employing the same thermostat and barostat configurations as those used in the bulk electrolyte simulations. 2D H_2O number density distribution on the Zn (002) surface was analyzed by the Density Calculator program [70].

3 Results and Discussion

3.1 Solvation Structure and Adsorption Characteristics Investigations

To modulate the EDL structure, TGS was selected as an electrolyte additive owing to its abundant polar functional groups, namely multiple hydroxyl (–OH) and chlorine (–Cl) moieties, and its relatively large molecular size (Fig. S2). These structural features are expected to promote the spontaneous adsorption of TGS onto the Zn metal surface, where it can exert a pronounced steric hindrance effect [71–73]. This interaction is anticipated to significantly influence the interfacial configuration and disrupt the local H-bond network. Furthermore, TGS serves as a model additive for the construction of a transferable multiscale theoretical platform, enabling the systematic regulation of EDL structures in electrochemical systems. Specifically, 2 M $ZnSO_4$ (ZS) electrolytes with different concentrations of TGS (10/50/100 mM) were used to assemble Zn||Zn symmetric cells. Under the galvanostatic condition of 1 mA cm^{-2} and 1 mAh cm^{-2}, the sample with 50 mM TGS exhibits an exceptionally stable cycle life exceeding 4700 h (Fig. S3). In comparison, the cell containing 10 mM TGS demonstrates an extended lifespan of approximately 4060 h, while it encounters a soft short circuit at around 3860 h [74]. Moreover, when the concentration of TGS is further increased to 100 mM, the cycling lifespan is markedly shortened to approximately 500 h. This degradation in performance is primarily attributed to a pronounced decrease in bulk ionic conductivity and a substantial increase in interfacial impedance, as evidenced by Figs. S4 and S5. Based on these observations, an optimized TGS concentration of 50 mM in ZS (ZS/TGS) was selected for further investigation. We first explored the bulk electrolyte solvation structures using CMD simulations, as outlined in Figs. S6 and S7. Fig. 2a presents the radial distribution functions (RDFs) and coordination numbers (CNs) for Zn^{2+} in the ZS/TGS electrolyte. Notably, negligible changes in

© The authors https://doi.org/10.1007/s40820-025-01915-w

RDFs and CNs are observed compared to that of the ZS electrolyte (Fig. S8), indicating that TGS does not alter the primary solvation shell of Zn^{2+}. Specifically, the predominant solvation structures remain ~ 75% $Zn^{2+}(H_2O)_6$ and ~ 25% $Zn^{2+}(H_2O)_5SO_4^{2-}$ complexes in Fig. S9. The absence of TGS in the solvation shell can be rationalized by examining the relative free energy of Zn^{2+} solvation complexes based on ligand field effects (Fig. 2b) [48]. The formation of a $Zn^{2+}(H_2O)_5$TGS complex is associated with a higher relative free energy, calculated to be 6.91 kcal mol^{-1} compared with the much lower free energy of − 4.24 kcal mol^{-1} of $Zn^{2+}(H_2O)_5SO_4^{2-}$ complex. This significant difference in relative free energy compared with $Zn^{2+}(H_2O)_6$ indicates that the sulfate ion (SO_4^{2-}) is more easily involved in the first solvation shell of Zn^{2+} ion [47, 75]. Further corroboration of the minimal impact of TGS on the solvation structure is provided by the Raman spectra and nuclear magnetic resonance (NMR) results, as shown in Figs. 2c and S10. There is nearly no chemical shift for the stretching vibrations of O–H and SO_4^{2-} and the characteristic peaks of ^2H, indicating that TGS would not change the coordination environment of Zn^{2+} ions, which is consistent with the results in the Fourier transform infrared (FTIR) spectra (Fig. S11) and the theoretical analysis above. In spite of the conclusion drawn above that TGS does not significantly affect the solvation structures of Zn^{2+}, noticeable molecular aggregation of TGS was detected (Fig. S7b), which may impact the ion diffusion process [76]. As expected, the diffusion coefficients of Zn^{2+}, SO_4^{2-}, and H_2O in the bulk electrolyte decreased upon the introduction of TGS, as revealed by the mean squared displacement (MSD) analysis in Fig. S12, demonstrating the significant steric hindrance effect of aggregated TGS molecules. Notably, these findings are consistent with the previously observed decline in bulk ionic conductivity after introducing the TGS. Hereto, it is reasonable to conjecture that the TGS molecule may work on the surface because of the non-negligible steric hindrance effect.

To elucidate the molecular characteristics of TGS, we calculated its ESP using QC methods. Figs. 2d and S13 illustrate the ESP mappings of TGS and H_2O molecules, where the ESP minima regions (blue points) located near the atoms with negative ESP values (blue areas), such as oxygen and chlorine atoms, could be identified as nucleophilic (potential adsorption) sites [77–79]. The ESP extrema of specific potential adsorption sites are recorded in Table S1. Subsequently, DFT calculations were performed to investigate various adsorption configurations on the Zn (002) surface, which was selected due to its lowest surface energy, indicating it as the most thermodynamically stable facet [77]. The adsorption states were categorized as 'parallel', 'angle', and 'vertical', corresponding to the molecular orientations parallel to, at an angle with respect to, or perpendicular to the surface, respectively (Fig. 2e, f). The results reveal that the TGS molecule reaches the most stable adsorption state when it is parallel to the Zn (002) surface, as indicated by the more negative adsorption energies (~ − 0.97 eV) and smaller adsorption angles (~ 25°) compared with other configurations (Table S2). Moreover, the adsorption energies of all TGS configurations were found to be higher than those of H_2O at the TOP, Bridge, HCP, and FCC sites (Figs. 2f and S14), highlighting the stronger binding affinity of TGS molecules to the Zn metal surface. Noticeably, the adsorption sites of TGS and H_2O molecules are both consistent with the predictions of QC calculations before (mark potential adsorption sites with blue dot rings).

With the revelation of the specific adsorption behavior and conditions for the TGS and H_2O molecules on the Zn metal surface by QC and DFT calculations, we further performed spectroscopy analyses to verify the interaction between the TGS molecule and the Zn anode. Fig. 2g presents the FTIR spectra of the Zn anode soaked in the ZS/TGS electrolyte for 3 days. The adsorbed peaks at ≈2900, ≈1000, and 700−750 cm^{-1} correspond to the stretching vibrations of C–H, C–O, and C–Cl from the TGS molecule, respectively [80], explicitly indicating the spontaneous adsorption of TGS on the Zn anode in aqueous solutions. The X-ray photoelectron spectroscopy (XPS) results collected in Figs. 2h, S15, and S16 provide additional confirmation of TGS adsorption. For the Zn anode soaked in ZS/TGS electrolytes for 3 days (Fig. 2h), distinct Cl peaks are observed at the binding energies of 199.7 eV (Cl $2p_{3/2}$) and 201.2 eV (Cl $2p_{1/2}$) [81], elaborating the presence of chlorine atoms bonded to sp^2 carbons. In addition, the introduction of TGS molecules reduces the contact angle of the electrolyte on the Zn foil from 78.3° to 67.4° (Fig. S17), signifying a marked improvement in surface wettability and the strong adsorption capability of TGS molecules on the Zn surface [82, 83]. Of note, the surface charge state of the Zn anode is identified by average differential areal capacity ($\overline{C}$), as shown in Figs. 2i, S18 and S19. The $\overline{C}$ is closely relevant to the EDL structure [84, 85], which can be derived from the following equation:

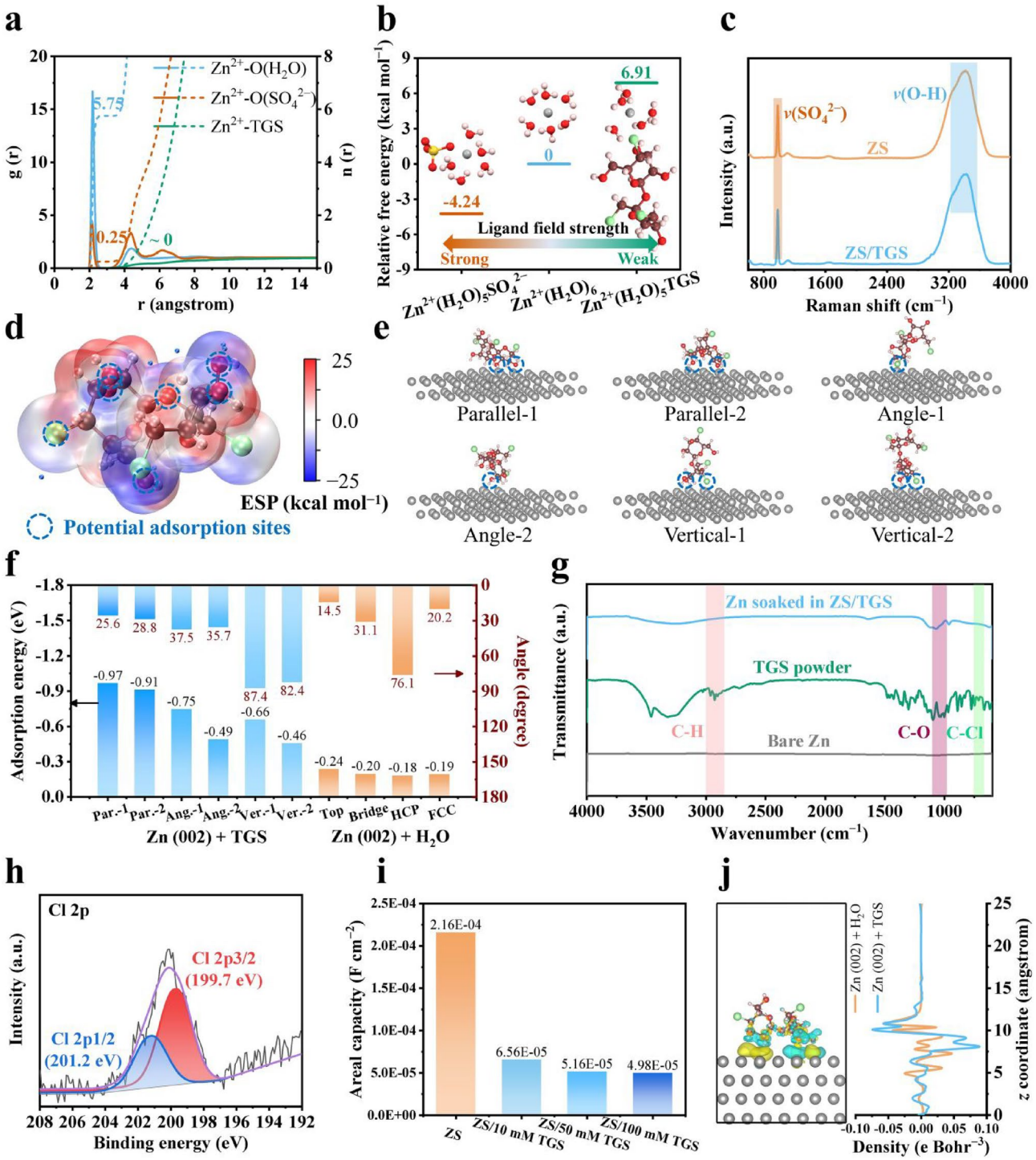

Fig. 2 Solvation structure and adsorption characteristics investigations. **a** RDFs and CNs of bulk electrolytes after the introduction of TGS. **b** Relative free energy comparison of $Zn^{2+}(H_2O)_5SO_4^{2-}$, $Zn^{2+}(H_2O)_6$, and $Zn^{2+}(H_2O)_5TGS$ complexes. **c** Raman spectra show characteristic vibrational modes in different electrolytes. **d** ESP mapping of TGS, with blue dotted rings marking potential adsorption (nucleophilic) sites. **e** Various adsorption configurations of TGS on the Zn (002) surface. **f** Adsorption energy and adsorbate–surface angles for different configurations of TGS and H_2O on the Zn (002) surface. **g** FTIR spectra of Zn foil soaked in ZS/TGS electrolyte for 3 days, compared with TGS powder, indicate the adsorption of TGS on the Zn surface. **h** XPS Cl 2p spectra of Zn foils soaked in the ZS/TGS electrolyte for 3 days. **i** Average differential capacitance comparison of Zn anodes in different electrolytes. **j** CDD distribution plots of Zn (002) + TGS and the 2D planar-average CDD plots (isovalue = 5×10^{-4} e Bohr^{-3}). The yellow and cyan iso-surfaces represent regions of increased and decreased charge density, respectively

© The authors https://doi.org/10.1007/s40820-025-01915-w

$$\bar{i} = \overline{C} \cdot v$$

where $\bar{i}$ is the average current density and v is the corresponding scan rate of the cyclic voltammetry (CV) curve. The introduction of TGS at varying concentrations leads to a notable decrease in $\overline{C}$ resulting in a water-poor EDL [85, 86]. Specifically, the capacitance drops significantly from 2.16×10^{-4} F cm^{-2} for the ZS electrolyte to 5.16×10^{-5} F cm^{-2} upon the addition of 50 mM TGS. However, further increase in the TGS concentration from 50 to 100 mM results in only a marginal change in capacitance (from 5.16×10^{-5} to 4.98×10^{-5} F cm^{-2}), indicating that the adsorption of Zn surface becomes saturated with 50 mM TGS additive. Moreover, the decrease in zeta potential indicates a less negatively charged Zn surface with the presence of TGS (Fig. S20), likely driven by the adsorption of TGS molecules and their influence on the surface charge distribution or potential. On this basis, the charge density difference (CDD) distribution plots provide deeper insights into the adsorption characteristics of TGS and H_2O on the Zn (002) surface, as showcased in Figs. 2i and S21. Much more dramatic charge exchanges between TGS and Zn (002) surface than those of H_2O are witnessed, verifying the stronger chemisorption and surface charge transfer.

While QC and DFT calculations, supported by experimental results, have successfully elucidated the specific adsorption behavior of TGS molecules and proved the reorganization of EDL, inherent limitations are inescapable with regard to these approaches [87]. Specifically, experimental techniques provide only a macroscopic perspective of the AEI, whereas QC and DFT calculations are confined to the analysis of individual TGS and H_2O molecules, overlooking the effects of molecular aggregation and orientation distribution [76]. Consequently, the EDL portrayed by these methods is incomplete. To overcome this limitation, CMD simulations were harnessed by the constant charge method (CCM) [88]. This approach endowed us with a systematic perspective on the interfacial behavior of TGS and H_2O molecules on the Zn metal surface under realistic electrolyte conditions. By leveraging this computational framework, we aim to provide a comprehensive clarification of the structural and functional intricacies of the EDL and unravel the role of TGS additives in modulating interfacial properties.

3.2 Dissection of the Electric Double Layers

Firstly, Fig. 3a–d illustrates the EDL structures of the Zn (002) surface in the ZS electrolyte, analyzed through CMD simulations (detailed simulation steps and structures are shown in Figs. S22 and S23, Table S3). Fig. 3a shows a snapshot from CMD simulations, where the interfacial region exhibits distinct layering of H_2O molecules and SO_4^{2-} ions near the Zn surface. This interfacial structure is quantitatively characterized in Fig. 3b, which presents the number density profiles of H_2O molecules and SO_4^{2-} ions as a function of the distance from the Zn surface. Accordingly, there are three interfacial zones based on the classical BDM model: (I) H_2O molecules and partial SO_4^{2-} ions directly adsorbed on the Zn surface (IHP, blue zone); (II) dominated by loosely associated water and SO_4^{2-} ions (OHP, orange zone); and (III) the diffuse layer (DL, yellow zone), where the ion concentrations gradually recover back to that of the bulk electrolyte. In the IHP, the tight and ordered adsorption of water molecules onto the Zn surface results in a pronounced first peak in the H_2O number density, reaching its maximum value. This indicates strong electrostatic interactions between the H_2O dipoles and Zn metal surface, leading to a well-organized interfacial water layer (Fig. S24). Moving into the OHP, the solvated $Zn^{2+}(H_2O)_6$ ions disrupt the orderliness of water molecules, resulting in a more loosely bound configuration, as demonstrated by a rapid decline in the H_2O number density. Concurrently, the larger OHP region allows more SO_4^{2-} ions to penetrate and adsorb onto the Zn surface. As a result, the number density of SO_4^{2-} ions exhibits a sharp increase from IHP to OHP and reaches a first peak in the number density profiles. At the boundary between the OHP and the DL, electrostatic interactions between H_2O molecules and SO_4^{2-} ions lead to a secondary peak in the number density profiles for both species [89, 90], corresponding to a region where water molecules and SO_4^{2-} ions achieve a local maximum in their spatial distributions due to mutual electrostatic stabilization. In the DL, the concentration of H_2O molecules gradually decreases as it transitions into the bulk electrolyte, where the structure becomes ordered. Similarly, the SO_4^{2-} ion concentration experiences slight fluctuations, ultimately reaching the homogeneous bulk electrolyte value. Further insights into the spatial arrangement of interfacial water are provided by the 2D number density distribution of H_2O molecules. As shown in Fig. 3c, a mass of water molecules is uniformly distributed across the Zn metal surface in the ZS electrolyte, indicating the isotropic water alignment on the Zn metal surface (Fig. S24). A conceptual summary of these findings is presented in Fig. 3d. In traditional ZS electrolytes,

a significant accumulation of ordered H_2O molecules and SO_4^{2-} anions occurs in the IHP and forms a water-rich and anion-adsorbed EDL structure, dramatically promoting undesirable side reactions, including HER and the formation of by-products such as ZSH. As SO_4^{2-} anions adsorb, they bring the negative charge closer to the electrode surface. In classical GCS models, the potential at the IHP is usually assumed to decrease relatively smoothly from the electrode potential to that of the bulk solution. However, the adsorbed anions create localized regions of high charge density. This can cause an immediate drop (or more pronounced "step") in potential near the IHP because the electrode now faces a layer of fixed negative charges based on the BDM model (as depicted in Fig. S1). Therefore, the presence of specifically adsorbed anions can produce a more abrupt change in potential, often a steeper initial decrease followed by a more gradual decay through the diffuse layer, which could lead to non-uniform Zn^{2+} ion depositions [75, 91].

By contrast, Fig. 3e–h highlights the impact of TGS molecule adsorption on the Zn metal surface, leading to a reconstructed EDL and the creation of a water-poor interfacial environment. Figs. 3e and S25 demonstrate the adsorption and aggregation of TGS molecules in IHP and OHP. This structural transformation is quantitatively depicted in Fig. 3f. Due to the robust adsorption and aggregation of TGS on the Zn surface, the number density of H_2O molecules in the IHP is significantly reduced. Similarly, the repulsion of SO_4^{2-} ions away from the interfacial region leads to their lower density

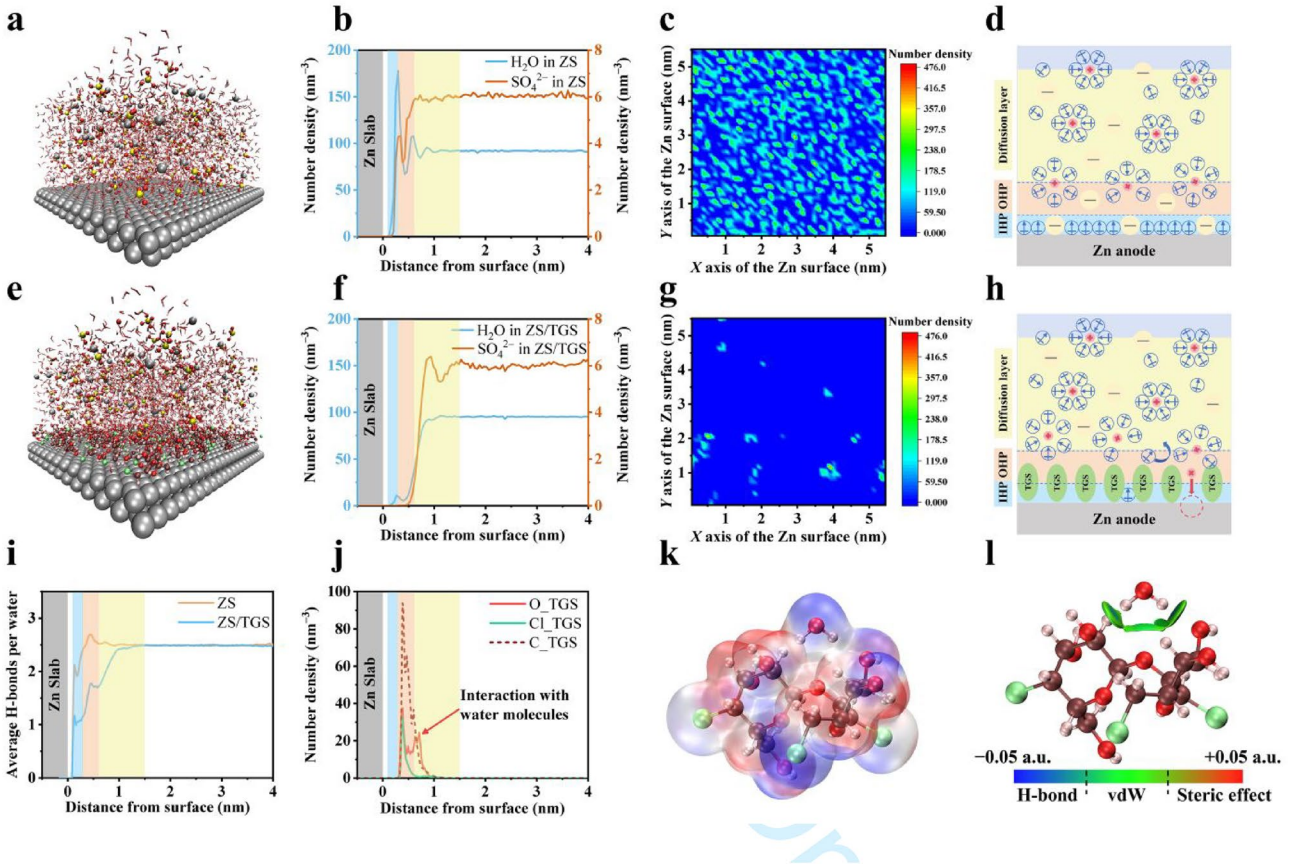

Fig. 3 Interfacial behavior of electrolytes on the Zn (002) surface. CMD simulation snapshots of **a** ZS and **e** ZS/TGS electrolytes on the Zn (002) surface, illustrating distinct interfacial structures. Number density profiles of H_2O and SO_4^{2-} ions as a function of distance from the Zn metal surface in **b** ZS and **f** ZS/TGS electrolytes, with interfacial zones labeled as IHP (blue zone), OHP (orange zone), and DL (yellow zone). 2D number density distributions of H_2O molecules on the Zn metal surface for **c** ZS and **g** ZS/TGS systems. Schematic diagrams of the EDL structures in **d** ZS and **h** ZS/TGS electrolytes. **i** Average H-bond number per water molecule as a function of distance from the Zn (002) surface. **j** Number density distributions of specific elements in TGS (O, Cl, and C) near the Zn (002) surface. **k** ESP mapping of the TGS + H_2O system, consistent with the color bar of Fig. 2d. **l** IGMH analysis of TGS + H_2O interactions, indicating vdW and weak H-bond interactions

© The authors
https://doi.org/10.1007/s40820-025-01915-w

in the HP. The 2D number density distribution of water molecules, as shown in Fig. 3g, further highlights this TGS molecular aggregation effect. Compared to the relatively uniform distribution observed in the ZS system (Fig. 3c), the TGS-modified interface exhibits sparse and localized H_2O adsorption, confirming the broken water layer structure and surface H-bond network [92]. To further evaluate molecular coverage, the surface coverage (θ) of TGS is defined by:

$$\theta = 1 - \frac{n'_{H_2O}}{n_{H_2O}}$$

where n_{H_2O} and n'_{H_2O} represent the relative molecule number of H_2O on the surface before and after TGS adsorption. The θ of TGS molecules reached 94.44%, indicating highly uniform adsorptions on the surface in a parallel configuration, which is consistent with the adsorption states predicted by previous DFT calculations. The schematic diagram in Fig. 3h summarizes the reconstructed EDL structure in the TGS-modified electrolyte. According to the Derjaguin-Landau-Verwey-Overbeek (DLVO) theory [93–95], the interactions between Zn^{2+} ion deposits in aqueous electrolytes are determined by the interplay between vdW attractive forces and the electrostatic repulsion arising from the EDL (Fig. S26). In ZS electrolytes, the strong EDL repulsion, driven by SO_4^{2-} counterions near the HP, leads to scattered and loose platelet-like Zn deposition [96]. The introduction of TGS molecules effectively repels SO_4^{2-} ions from the HP, reducing the surface charge density and redistributing the potential drop within the EDL (Fig. S27), which is consistent with the decrease in zeta potential. In other words, the energy barrier of the Zn^{2+} ion deposit could be reduced by lowering the net charges of particles. Furthermore, TGS flattens the potential profile and weakens the electrostatic repulsion between Zn^{2+} ion deposits, allowing the vdW force to dominate, which promotes dense and coherent deposition processes. These structural and electrostatic modifications improve the morphology of Zn^{2+} ion deposits, as discussed in the later section.

As is well known, the activity of H_2O molecules primarily depends on the intensity of the H-bond network formed between the H and O atoms of adjacent H_2O and directly affects the side reactions of H_2O decomposition [97]. Fig. 3i quantifies the average number of H-bonds per water molecule on the Zn surface for both ZS and ZS/TGS electrolytes. In the presence of TGS, the number of H-bonds per water decreases significantly, dropping from 2.1 to 1.1 in the IHP and from 2.6 to 1.7 in the OHP, which reflects the disruption of the H-bond network at the EDL caused by TGS adsorption. This result is also observed from surface structure snapshots (Fig. S28), breaking the continuous H-bond network in the ZS/TGS electrolyte. Fig. 3j highlights that those electron-rich atoms (such as O and Cl) from the TGS molecule would effectively participate in the IHP and OHP region and modify the EDL structure, due to their strong affinity to the Zn surface (Fig. 2e). At the same time, partial O atoms in TGS could interact with water molecules to avoid them in the HP. To further investigate the interactions between TGS and H_2O molecules, ESP mapping of the TGS + H_2O system was performed, as shown in Fig. 3k. The ESP mapping reveals intensive interactions between TGS and H_2O molecules. Specifically, the nucleophilic site of TGS (three oxygen atoms) can bind well to the electrophilic site of H_2O molecules (two hydrogen atoms) and further change the electrostatic potential at the binding site. This is further supported by the binding energy calculations (Fig. S29), as shown that the TGS-H_2O interaction (-9.90 kcal mol^{-1}) is much stronger than that of H_2O-H_2O (-5.14 kcal mol^{-1}). Moreover, the IGMH analysis is conducted to provide deeper insight into TGS-H_2O interactions (Figs. 2l and S30) [44]. The IGMH visualization identifies vdW interactions and weak H-bonds as the key stabilizing factors between TGS and H_2O molecules [98]. As a result, the complex interactions between TGS and H_2O molecules significantly break the H-bond network of H_2O at the interface and reduce the activity of free water, thus reconstructing a water-poor EDL with inhibited side reactions for the Zn anode.

To account for the potential-dependent behavior of the Zn metal anode, the Zn (002) surface was polarized from the PZC [99]. Charge distribution on the Zn (002) surface under varying polarization conditions was calculated using joint density functional theory (JDFT) [100, 101], as implemented in the JDFTx software [102]. Fig. S31 illustrates the variation in charge density on the Zn (002) surface as a function of potential relative to the PZC, serving as a foundation for understanding the interfacial behavior under different polarization conditions [31]. When the Zn surface potential is polarized to + 0.5 and − 0.5 V from the PZC, distinct adsorption phenomena are observed, as illustrated in Figs. S32-S35. Specifically, TGS molecules become continuously adsorbed and enriched on the Zn (002) surface under both positive and negative polarization conditions (Fig. S28). Figs. S33 and S34 also confirm the reduction in H_2O and SO_4^{2-} concentrations at the EDL, highlighting

the role of TGS in mitigating the undesired side reactions. Further analysis of the H-bond network on the Zn surface under different polarization conditions is also performed (Fig. S35). In ZS electrolytes, the average number of surface H-bonds displays distinct characteristics based on the applied potential. At + 0.5 V *vs.* PZC, the first peak of the H-bond count is lower than the bulk H-bond value, consistent with observations at the PZC situation, which reflects the relatively loose H_2O-H_2O interactions near the positively charged surface. Conversely, at − 0.5 V *vs.* PZC, the first peak of the H-bond count is higher than the bulk H-bond value. This increase results from the accumulation of negative charge, which promotes the ordered and compact arrangement of water molecules and enhances H-bond density. To be noted, the adsorption of TGS molecules on both sides can effectively reduce the number of H-bonds on the surface and change the local EDL environment. At − 0.5 V *vs.* PZC, the first peak of the H-bond count is significantly reduced after introducing TGS molecules, which is lower than the bulk H-bond numbers.

In summary, the CMD simulations and subsequent multi-dimensional analyses reveal that the introduction of TGS into the ZS electrolyte leads to significant reconstruction of the EDL at the Zn metal surface. TGS molecules preferentially adsorb onto the Zn surface, displacing H_2O molecules and SO_4^{2-} anions. This adsorption reduces surface H-bond and redistributes the potential drop, creating a water-poor and anion-expelled EDL environment that suppresses parasitic reactions and enhances the stability and performance of the Zn anode. Our coupled multiscale simulation platform provides a clear depiction of the EDL structure, ion/molecular distribution, and interfacial behaviors, seamlessly integrating QC, DFT, and CMD. This approach offers valuable insights into strategies for EDL regulation theoretically. Subsequent experimental results will further validate the accuracy and predictive phenomena of these theoretical calculations.

3.3 Evaluation of Anti-Corrosion and Deposition Kinetics of the Zn Anode

Based on the modified EDL structure with the addition of TGS, the corrosion resistance and deposition kinetics of the Zn anode were evaluated experimentally (Fig. 4). The scanning electron microscope (SEM) images and X-ray diffraction (XRD) patterns of the Zn foil soaked in ZS electrolyte for 3 days present obvious corrosion, characterized by randomly distributed irregular ZSH by-products and rough surface morphology, indicative of severe side reactions (Figs. 4a and S36) [103]. In sharp contrast, the Zn anode soaked in ZS/TGS electrolyte for the same condition exhibits a smoother and more uniform surface, without the distinct formation of by-products, confirming enhanced anti-corrosion of the Zn anode conferred by the TGS additive. Accordingly, the Tafel plots show a much lower corrosion current density for the ZS/TGS electrolyte compared to the ZS electrolyte (0.86 *vs.* 4.64 mA cm^{-2}, Fig. 4b). The linear sweep voltammetry (LSV) curves also take on a significantly reduced current density under the negative polarization region (Fig. 4c), which is attributed to the amplified energy barrier of HER after TGS adsorption (from 0.69 to 0.84 eV) based on DFT calculations (Fig. 4d). These results demonstrate that a water-poor and anion-expelled EDL constructed by adsorbed TGS would slow down the HER rate and enhance the stability of the Zn anode in a mild/acid aqueous system.

The chronoamperometry (CA) tests are performed to probe into the effect of the modified EDL on Zn^{2+} ion deposition behavior. Different from the random 2D diffusion in the ZS electrolyte, the ZS/TGS electrolyte promotes a uniform 3D diffusion of Zn^{2+} ions at the interface [72, 104], effectively preventing Zn dendritic growth and ensuring a more stable Zn^{2+} ion deposition process (Fig. 4e). As pointed out in the previous theoretical calculations, TGS will inevitably incur a strong steric hindrance effect on the surface, which is confirmed by the enlarged charge transfer resistance (R_{ct}) in the electrochemical impedance spectroscopy (EIS) spectra shown in Fig. S5 [71–73]. Additionally, the CV curves of Zn||Cu half cells demonstrate that the ZS/TGS electrolyte results in a postponed onset potential of Zn^{2+} ion deposition (Fig. 4f), indicating the significant polarization on the Zn anode. Furthermore, the activation energy (E_a) of the ZS/TGS electrolyte (83.35 kJ mol^{-1}) is slightly higher than that of the ZS electrolyte (77.29 kJ mol^{-1}) in Figs. S37 and S38, indicating that the presence of adsorbed TGS within the EDL slows Zn^{2+} diffusion at the Zn-electrolyte interface and moderates the Zn^{2+} deposition kinetics [105, 106]. This regulated ion transport promotes a more uniform Zn^{2+} flux, leading to dense and homogeneous Zn deposition. These findings are consistent with the increased

© The authors https://doi.org/10.1007/s40820-025-01915-w

interfacial polarization observed in the presence of the TGS additive.

The electrodeposition morphology of Zn in ZS and ZS/TGS electrolytes was systematically analyzed under varying current densities and areal capacities, as depicted in Fig. 4g, h. The overpotential (η_C) governing the electrodeposition process is expressed as [91]:

$$\eta_C = \phi_1 + \frac{2RT}{F} \ln j_C$$

where ϕ_1 represents the potential of the diffuse layer, R is the ideal gas constant, T is the absolute temperature, F is the Faraday constant, and j_C is the exchange current density. The repulsion of SO_4^{2-} ions in HP leads to a redistribution of anions further into the diffuse layer, effectively lowering the potential gradient in this region. As a result, the weaker potential drop in HP gives rise to an increase in the potential of the diffuse layer (ϕ_1) in Fig. S27. The increased ϕ_1 brings about a higher overpotential, which is beneficial to uniform and compact Zn^{2+} ion deposition as it reduces the critical nucleation size and increases nucleation density [71].

At a current density of 1 mA cm^{-2} and an areal capacity of 1 mAh cm^{-2}, the electrodeposition morphology in ZS electrolyte exhibits a rough and porous mossy structure, indicative of severe HER and dendrite growth (Fig. 4g)

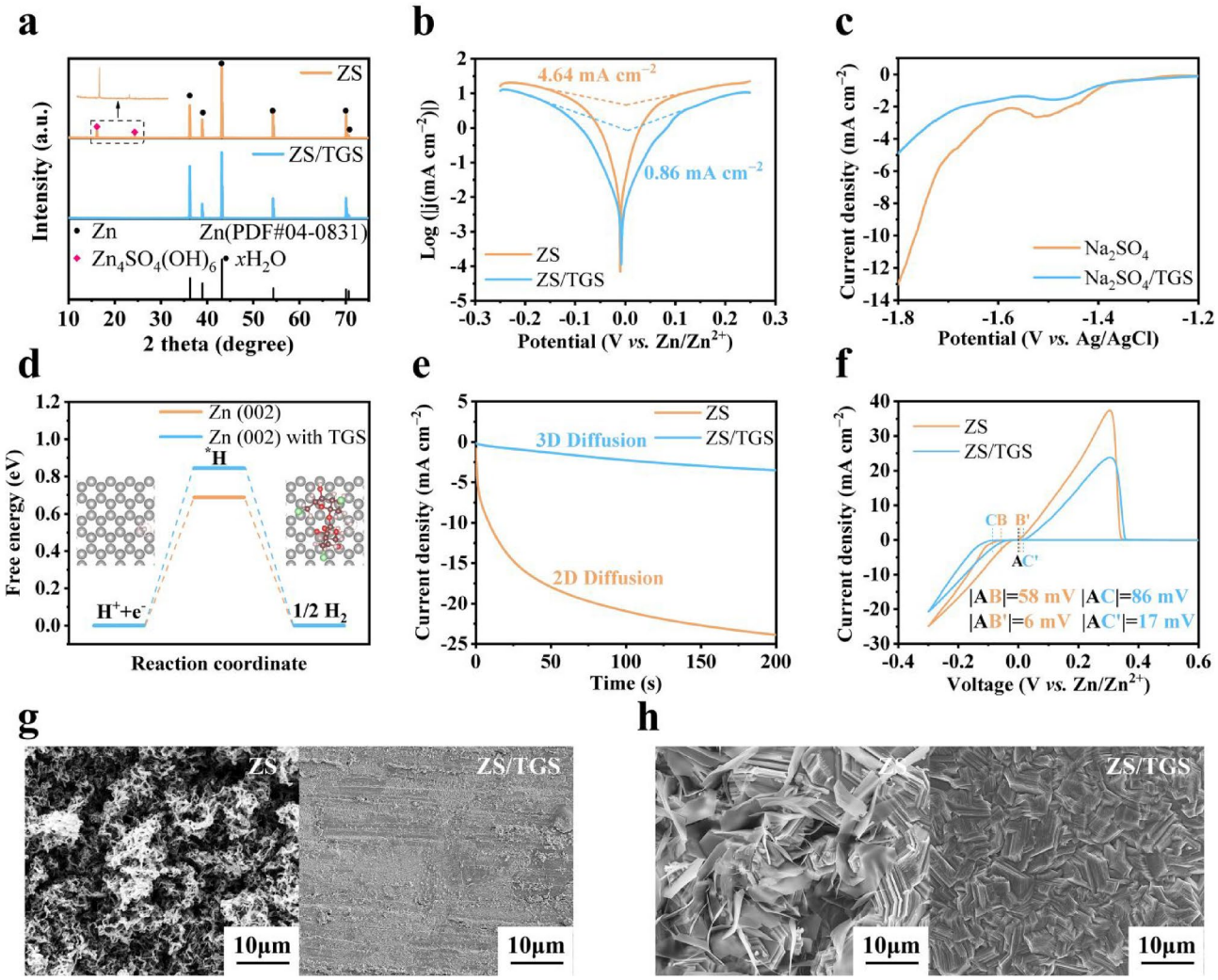

Fig. 4 Evaluation of anti-corrosion and deposition kinetics of the Zn anode. **a** XRD patterns of the immersed Zn foils for 3 days, with the ZS sample showing peaks of ZSH corrosion by-products, absent in ZS/TGS. **b** Tafel plots of Zn||Zn symmetric cells. **c** LSV curves of three-electrode beaker cells indicate reduced hydrogen evolution in ZS/TGS compared to ZS. **d** Calculated HER energy barriers showing higher barriers for Zn (002) with TGS. **e** CA curves at an overpotential of −150 mV. **f** CV curves of Zn||Cu asymmetric cells. SEM images of Zn electrodeposited on Zn substrates at **g** 1 mA cm^{-2}, 1 mAh cm^{-2} and **h** 4 mA cm^{-2}, 2 mAh cm^{-2} in ZS and ZS/TGS electrolytes

[107]. The morphology of initial Zn nucleation critically influences the subsequent growth behavior, playing a pivotal role in dendrite formation and ultimately affecting the long-term cycling stability and lifespan of the battery [108, 109]. This irregular morphology can compromise the stability of the Zn anode and lead to a rapid short circuit because of strong EDL repulsion according to DLVO theory. In contrast, the Zn anode in the ZS/TGS electrolyte takes on a much smoother and more uniform surficial morphology under identical conditions, as exhibited due to the vdW force domination. At a higher current density of 4 mA cm^{-2} and an areal capacity of 2 mAh cm^{-2}, the Zn^{2+} ion deposits in the ZS electrolyte display pronounced dendritic structures with large sharp-edge plates, while remaining smooth and compact in the ZS/TGS electrolyte, with a well-defined and uniform crystalline structure (Fig. 4h). Additional electrodeposition morphologies at higher current densities and areal capacities (5 mA cm^{-2}, 2.5 mAh cm^{-2}; 5 mA cm^{-2}, 5 mAh cm^{-2}) are presented in Figs. S39 and S40, which reveal similar trends. Accordingly, it is reasonable to claim that incorporating TGS into the ZS electrolyte moderates the Zn^{2+} ion deposition kinetics, leading to a homogeneous and dense growth of electrodeposition.

3.4 Modified EDL Induced Superior Electrochemical Performance

We then assessed the reversibility of the Zn anode in ZS and ZS/TGS electrolytes by measuring the CE in Zn||Cu asymmetric cells. As shown in Fig. 5a, at a current density of 1 mA cm^{-2} and an areal capacity of 0.5 mAh cm^{-2}, the Zn||Cu cell with ZS electrolyte operates only 200 cycles and then reaches a short circuit. In sharp contrast, the cell utilizing ZS/TGS electrolyte exhibits stable cycling for over 1100 cycles, achieving an impressive average CE of 99.49%. Even at a higher current density of 4 mA cm^{-2} and an areal capacity of 1 mAh cm^{-2}, the cell with ZS/TGS electrolyte can still stably cycle for up to 700 cycles with a superior CE of 99.59% (Fig. 5b), observably outperforming that of the cell with ZS electrolyte. The promotion in CE embodies optimized Zn plating/stripping reversibility achieved by TGS-regulated EDL structure. To further verify the long-term cycling stability of the Zn anode, we perform the galvanostatic charge/discharge tests of Zn||Zn symmetric cells in both electrolytes. As shown in Fig. 5c, the Zn anode in the ZS/TGS electrolyte demonstrates significantly prolonged cycling stability for over 4700 h compared to only 140 h in the ZS electrolyte, under a current density of 1 mA cm^{-2} and an areal capacity of 1 mAh cm^{-2}. To gain deeper insights into the morphological evolution of the Zn anode, the Zn anodes cycled for 10, 20, and 30 cycles in ZS and ZS/TGS electrolytes at the same condition are characterized by SEM (Fig. 5d). The Zn anode cycled in ZS/TGS electrolyte delivers a uniform and smooth Zn plating/stripping process, further confirming the effect of EDL reconstruction in facilitating the homogeneous Zn^{2+} ion deposition by amplifying the overpotential (~ 100 mV at 1 mA cm^{-2} and 1 mAh cm^{-2}). However, in the ZS electrolyte, the cycled Zn anode exhibits non-uniform plating/stripping, inducing noticeable voids and randomly distributed Zn sheets. Moreover, similar results are shared by the Zn anodes cycled under other conditions, as presented in Figs. S41-S43. The XRD patterns in Fig. S44 further confirm the formation of ZSH after 30 cycles at 1 mA cm^{-2} and 1 mAh cm^{-2} in the ZS electrolyte. Optical photographs of the ZS electrolyte post-cycling reveal noticeable dead Zn, while the ZS/TGS electrolyte remains transparent (Fig. S44b, c). At a higher current density of 4 mA cm^{-2}, the Zn anode in the ZS/TGS electrolyte still operates stably for up to 1100 h, approximately six times longer than that in the ZS electrolyte (~ 180 h, Fig. 5e). Additional long-term cycling tests at various conditions (4 mA cm^{-2} and 2 mAh cm^{-2}; 5 mA cm^{-2} and 1 mAh cm^{-2}) also demonstrate the superior performance of the ZS/TGS electrolyte (Fig. S45). To evaluate the rate performance of symmetric cells, Zn||Zn cells were tested at current densities ranging from 0.5 to 10 mA cm^{-2}, as shown in Fig. S46. As expected, the cell using the ZS electrolyte experienced a short circuit when the current density was returned to 0.5 mA cm^{-2}. In contrast, the cell with the ZS/TGS electrolyte maintained stable cycling across all current densities, with a noticeably increased overpotential compared to the ZS electrolyte. In the under-limiting current region, the cells can operate safely without reaching the limit of mass transfer. In this regime, nucleation theory plays a dominant role, higher overpotential, along with the increased interfacial impedance observed for the ZS/TGS electrolyte, facilitates more stable Zn deposition and suppresses side reactions [71, 110]. Impressively, under a harsh circumstance of 50% Zn utilization rate (depth of discharge, DOD_{Zn}), the Zn||Zn symmetric cell with ZS/TGS electrolyte shows extended lifespan

© The authors https://doi.org/10.1007/s40820-025-01915-w

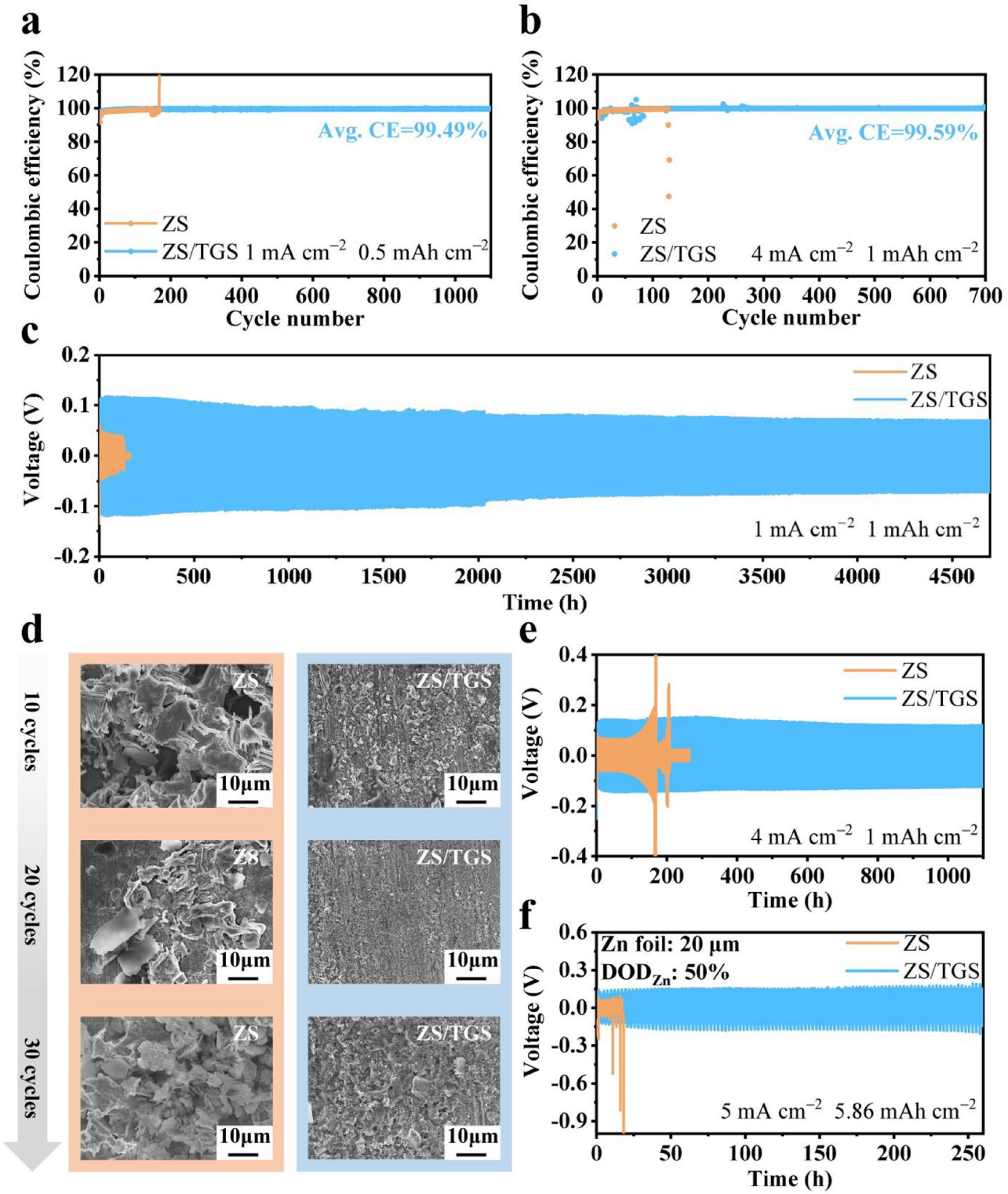

Fig. 5 Reversibility evaluation of Zn anode. CE comparisons of Zn||Cu asymmetric cells at **a** 1 mA cm^{-2}, 0.5 mAh cm^{-2} and **b** 4 mA cm^{-2}, 1 mAh cm^{-2}. **c** Voltage profiles of Zn||Zn symmetric cells galvanostatically cycled at 1 mA cm^{-2}, 1 mAh cm^{-2}, showing stable cycling in ZS/TGS over 4700 h. **d** SEM images of cycled Zn foils after 10, 20, and 30 cycles (1 mA cm^{-2}, 1 mAh cm^{-2}) in ZS (left, orange background) and ZS/TGS (right, blue background) electrolytes. Voltage profiles of Zn||Zn symmetric cells galvanostatically cycled at **e** 4 mA cm^{-2}, 1 mAh cm^{-2} and at **f** 5 mA cm^{-2}, 5.86 mAh cm^{-2} (DOD_{Zn} = 50%)

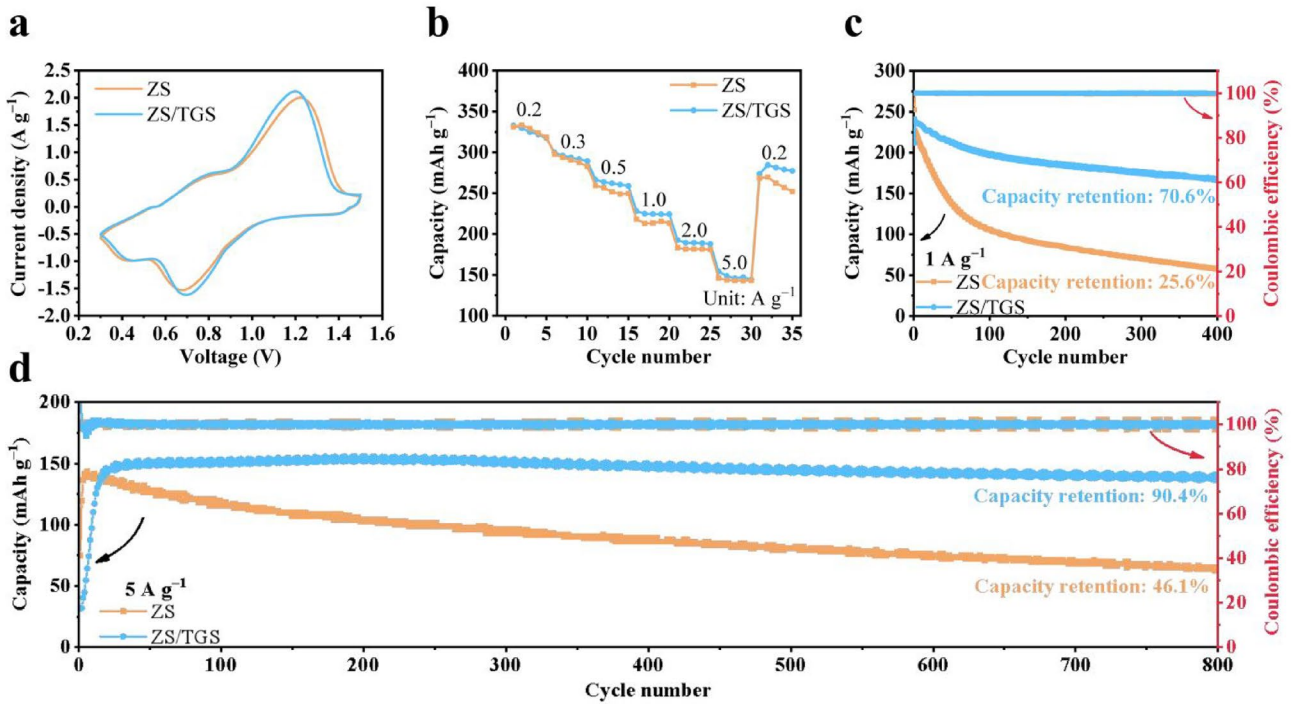

Fig. 6 Electrochemical performance of Zn||NVO full cells in different electrolytes. **a** CV curves of Zn||NVO full cells. **b** Rate performance at varying current densities (initial five cycles excluded from rate analysis due to the activation process). Long-term cycling performance of Zn||NVO at **c** 1 A g^{-1} and **d** 5 A g^{-1}, indicating superior durability and reversibility in the ZS/TGS electrolyte system

to 260 h (Fig. 5f). In comparison, the Zn anode in the ZS electrolyte suffers from uneven nucleation and uncontrolled Zn/Zn^{2+} redox kinetics, accompanied by serious side reactions, leading to rapid active Zn consumption and perforation of the electrode, ultimately causing the cell to reach an open circuit within just 15 h. Finally, the cumulative plating capacity (CPC) at various current densities, 2.35 Ah cm^{-2} over 4700 h at 1 mA cm^{-2}, 2.2 Ah cm^{-2} over 1100 h at 4 mA cm^{-2}, and 1.65 Ah cm^{-2} over 660 h at 5 mA cm^{-2}, demonstrates the superior performance of our system, surpassing most previously reported additive-based strategies (Fig. S47).

To assess the practicality of regulating the EDL in real-world applications, Zn||NaV_3O_8•1.5H_2O (NVO) full cells were assembled. The SEM image and XRD pattern of the NVO powders (Figs. S48 and S49) confirm a nanobelt morphology and a highly crystalline phase, which can be indexed to the $P2_1/m$ space group (PDF#16-0601). EIS results for Zn||NVO full cells (Fig. S50) reveal a charge transfer resistance comparable to that observed in symmetric cells, which is consistent with the previous analysis of interfacial reaction kinetics. The CV profiles of Zn||NVO full cells with different electrolytes (Fig. 6a) reveal similar redox peaks, indicating that TGS primarily functions on the electrode surface without directly participating in the redox reactions of the NVO cathode during charge and discharge processes. This confirms that the improvements in cell performance originate from the regulated EDL rather than changes in the cathode redox chemistry. Fig. 6b showcases the rate performance of the full cells. At low current densities (0.2 and 0.3 A g^{-1}), both ZS and ZS/TGS cells exhibit comparable capacities, as side reactions associated with vanadium dissolution from the cathode remain negligible in both systems. However, as cycling progresses under higher current densities (0.5-5 A g^{-1}), the ZS electrolyte suffers from persistent side reactions that progressively degrade the NVO cathode, leading to diminished capacity and inferior rate performance. In contrast, the ZS/TGS full cell consistently delivers higher capacity and superior rate capability, highlighting the effectiveness of the TGS-modulated interfacial environment. This enhancement is attributed to the preferential adsorption of TGS on both the anode and cathode surfaces, where it facilitates the formation of a "water-poor and anion-expelled" EDL. By suppressing water insertion and

© The authors
https://doi.org/10.1007/s40820-025-01915-w

anion accumulation at the interface, vanadium dissolution is significantly mitigated, thereby preventing the formation of inactive by-products and enabling more stable electrochemical kinetics [111, 112]. Long-term cycling performance at 1 A g^{-1} (Fig. 6c) highlights the differences between the ZS and ZS/TGS systems. The ZS-based full cell undergoes an activation process within the first 2 cycles, reaching a peak specific capacity of 226 mAh g^{-1} before rapidly declining to 25.6% of the initial capacity after 400 cycles due to the severe side reactions at low rates [20]. In contrast, the ZS/TGS-based full cell retains 70.6% of its original capacity (168 mAh g^{-1}) after 400 cycles, manifesting the stability provided by the TGS adsorption-regulated EDL structure. At a higher rate of 5 A g^{-1} (Fig. 6d), a longer activation process, typically spanning 5 to 30 cycles, is required. This behavior is attributed to intensify interfacial polarization, elevated Zn^{2+} flux, and increased overpotential, all of which collectively delay the formation of a stable EDL and uniform Zn deposition. Nevertheless, the ZS/TGS-based full cell demonstrates excellent long-term stability, retaining 90.4% of its capacity and delivering 141 mAh g^{-1} even after 800 cycles. By contrast, the ZS-based cell suffers from a drastic decline in specific capacity to 46.1% within 800 cycles, primarily due to irreversible capacity loss caused by severe side reactions. To evaluate practical applicability, a single-layer Zn||NVO pouch cell with cathode mass loadings of 20 mg cm^{-2} was assembled, as illustrated in Fig. S51. The 0.24 Ah single-layer pouch cell utilizing the TGS-containing electrolyte demonstrates an extended cycling lifespan of over 50 cycles at a small current density of 0.1 A g^{-1} (2 mA cm^{-2}), retaining 71.8% of its initial capacity.

4 Conclusions

This study establishes a multiscale computational framework integrating QC, DFT, and CMD to comprehensively elucidate the interfacial mechanisms governing the stability and reversibility of Zn anodes in ARZBs. By synergistically bridging ab initio molecular-level insights with experimental validation, this framework resolves the dynamic evolution of the EDL under operational conditions, offering unprecedented clarity on the interplay between interfacial chemistry and electrochemical performance. QC simulations identified critical adsorption sites on Zn surfaces, while DFT calculations quantified the energetics and configurations of adsorbate interactions, revealing the preferential adsorption of TGS molecules. CMD simulations further uncovered the EDL's structural reorganization under realistic electrolyte conditions, demonstrating how TGS disrupts the native water-rich and anion-dense interfacial environment. The combined theoretical analyses established that TGS adsorption induces steric hindrance and site-specific interactions, effectively expelling free water and anions from the EDL. This restructuring suppresses parasitic reactions (e.g., hydrogen evolution, by-product formation) and promotes uniform Zn^{2+} ion deposition by homogenizing interfacial ion flux. Experimental validation corroborated these theoretical predictions: Zn||Zn symmetric cells with TGS-modified electrolytes achieved ultralong cycling stability (> 4700 h at 1 mA cm^{-2}/1 mAh cm^{-2}), while Zn||Cu asymmetric cells exhibited a superior CE (99.49% over 1100 cycles at 1 mA cm^{-2}/0.5 mAh cm^{-2}). Full cells paired with NVO cathodes retained 90.4% capacity retention after 800 cycles at 5 A g^{-1}, underscoring the practical viability of the TGS additive. These results not only validate the predictive power of the multiscale framework, but also highlight its utility in guiding the rational design of electrolyte additives for next-generation ARZBs.

Acknowledgements This work was supported by the National Natural Science Foundation of China (52471240), the Natural Science Foundation of Zhejiang Province (LZ23B030003), and the Fundamental Research Funds for the Central Universities (226-2024-00075). Y. X. thanks Prof. Tingting Shi (Jinan University) for helpful support and suggestions. B. B. X. is grateful for the support from the Engineering and Physical Sciences Research Council (EPSRC, UK) RiR grant - RIR18221018-1 and EU COST CA23155. Y. X. and Z. L. contributed equally to this work.

Author Contributions Yufan Xia was involved in investigation, simulation, visualization, characterization, data interpretation, and original draft writing. Zhen Luo was involved in investigation, visualization, characterization, and original draft writing. Shuang Chen was involved in data interpretation and mechanism discussion. Yang Xiang was involved in characterization and mechanism discussion. Gao Weng was involved in mechanism discussion. Hongge Pan, Ben Bin Xu, and Mi Yan were involved in review. Yinzhu Jiang was involved in conceptualization, investigation, review, supervision, funding acquisition, and revision.

Declarations

Conflict of interest The authors declare no conflict of interest. They have no known competing financial interests or personal relationships that could have appeared to influence the work reported in this paper.

Open Access This article is licensed under a Creative Commons Attribution 4.0 International License, which permits use, sharing, adaptation, distribution and reproduction in any medium or format, as long as you give appropriate credit to the original author(s) and the source, provide a link to the Creative Commons licence, and indicate if changes were made. The images or other third party material in this article are included in the article's Creative Commons licence, unless indicated otherwise in a credit line to the material. If material is not included in the article's Creative Commons licence and your intended use is not permitted by statutory regulation or exceeds the permitted use, you will need to obtain permission directly from the copyright holder. To view a copy of this licence, visit http://creativecommons.org/licenses/by/4.0/.

Supplementary Information The online version contains supplementary material available at https://doi.org/10.1007/s40820-025-01915-w.

References

1. H. Wan, Z. Wang, W. Zhang, X. He, C. Wang, Interface design for all-solid-state lithium batteries. Nature **623**(7988), 739–744 (2023). https://doi.org/10.1038/s41586-023-06653-w
2. V.R. Stamenkovic, D. Strmcnik, P.P. Lopes, N.M. Markovic, Energy and fuels from electrochemical interfaces. Nat. Mater. **16**(1), 57–69 (2016). https://doi.org/10.1038/nmat4738
3. X. Wang, M. Salari, D.-E. Jiang, J. Chapman Varela, B. Anasori et al., Electrode material–ionic liquid coupling for electrochemical energy storage. Nat. Rev. Mater. **5**(11), 787–808 (2020). https://doi.org/10.1038/s41578-020-0218-9
4. C. Zhang, M.F. Calegari Andrade, Z.K. Goldsmith, A.S. Raman, Y. Li et al., Molecular-scale insights into the electrical double layer at oxide-electrolyte interfaces. Nat. Commun. **15**(1), 10270 (2024). https://doi.org/10.1038/s41467-024-54631-1
5. S.-J. Shin, D.H. Kim, G. Bae, S. Ringe, H. Choi et al., On the importance of the electric double layer structure in aqueous electrocatalysis. Nat. Commun. **13**, 174 (2022). https://doi.org/10.1038/s41467-021-27909-x
6. W. Schmickler, Double layer theory. J. Solid State Electrochem. **24**(9), 2175–2176 (2020). https://doi.org/10.1007/s10008-020-04597-z
7. N.M. Markovic, Interfacing electrochemistry. Nat. Mater. **12**(2), 101–102 (2013). https://doi.org/10.1038/nmat3554
8. P. Attard, Electrolytes and the electric double layer. Adv. Chem. Phys. **92**, 1–159 (1996). https://doi.org/10.1002/9780470141519
9. H. Helmholtz, Ueber einige Gesetze der Vertheilung elektrischer Ströme in körperlichen Leitern mit Anwendung auf die thierisch-elektrischen Versuche. Ann. Der Phys. **165**(6), 211–233 (1853). https://doi.org/10.1002/andp.18531650603
10. O. Stern, Zur theorie der elektrolytischen doppelschicht. Z. Für Elektrochem. Und Angew. Phys. Chem. **30**(21–22), 508–516 (1924). https://doi.org/10.1002/bbpc.192400182
11. N. Hu, W. Lv, W. Chen, H. Tang, X. Zhang et al., A double-charged organic molecule additive to customize electric double layer for super-stable and deep-rechargeable Zn metal pouch batteries. Adv. Funct. Mater. **34**(8), 2311773 (2024). https://doi.org/10.1002/adfm.202311773
12. J. Zhao, S. Ma, Z. Wang, Q. Gao, H. Xiao et al., Electrolyte-tailored heterostructured zinc metal anodes with tunable electric double layer for fast-cycling aqueous zinc batteries. Adv. Funct. Mater. **34**(46), 2405656 (2024). https://doi.org/10.1002/adfm.202405656
13. X. Shi, J. Xie, F. Yang, F. Wang, D. Zheng et al., Compacting electric double layer enables carbon electrode with ultrahigh Zn ion storage capability. Angew. Chem. Int. Ed. **61**(51), e202214773 (2022). https://doi.org/10.1002/anie.202214773
14. S. Li, J. Zhao, X. Xu, J. Shen, K. Zhang et al., Regulating interfacial behavior *via* reintegration the Helmholtz layer structure towards ultra-stable and wide-temperature-range aqueous zinc ion batteries. Mater. Today **80**, 50–60 (2024). https://doi.org/10.1016/j.mattod.2024.08.003
15. D.C. Grahame, The electrical double layer and the theory of electrocapillarity. Chem. Rev. **41**(3), 441–501 (1947). https://doi.org/10.1021/cr60130a002
16. J.O. Bockris, M.A.V. Devanathan, K. Müller, On the structure of charged interfaces. In: Electrochemistry. Elsevier, pp. 832–863 (1965). https://doi.org/10.1016/b978-1-4831-9831-6.50068-0
17. F. Wang, O. Borodin, T. Gao, X. Fan, W. Sun et al., Highly reversible zinc metal anode for aqueous batteries. Nat. Mater. **17**(6), 543–549 (2018). https://doi.org/10.1038/s41563-018-0063-z
18. J. Zhu, Z. Tie, S. Bi, Z. Niu, Towards more sustainable aqueous zinc-ion batteries. Angew. Chem. Int. Ed. **136**(22), e202403712 (2024). https://doi.org/10.1002/ange.202403712
19. S. Liu, R. Zhang, C. Wang, J. Mao, D. Chao et al., Zinc ion batteries: bridging the gap from academia to industry for grid-scale energy storage. Angew. Chem. Int. Ed. **136**(17), e202400045 (2024). https://doi.org/10.1002/ange.202400045
20. C. Li, S. Jin, L.A. Archer, L.F. Nazar, Toward practical aqueous zinc-ion batteries for electrochemical energy storage. Joule **6**(8), 1733–1738 (2022). https://doi.org/10.1016/j.joule.2022.06.002
21. W. Zhang, M. Dong, K. Jiang, D. Yang, X. Tan et al., Self-repairing interphase reconstructed in each cycle for highly reversible aqueous zinc batteries. Nat. Commun. **13**(1), 5348 (2022). https://doi.org/10.1038/s41467-022-32955-0
22. J.X.K. Zheng, J. Yin, T. Tang, L.A. Archer, Moss-like growth of metal electrodes: on the role of competing faradaic reactions and fast charging. ACS Energy Lett. **8**(5), 2113–2121 (2023). https://doi.org/10.1021/acsenergylett.3c00120
23. L. Jiang, D. Li, X. Xie, D. Ji, L. Li et al., Electric double layer design for Zn-based batteries. Energy Storage Mater. **62**, 102932 (2023). https://doi.org/10.1016/j.ensm.2023.102932

24. Y. Li, B. Ping, J. Qu, J. Ren, C. Lin et al., Constructing autoregulative electric double layer through dielectric effect toward fast charging zinc metal anode. Adv. Energy Mater. **15**(21), 2405804 (2025). https://doi.org/10.1002/aenm.202405804
25. L. Jiang, Y. Ding, L. Li, Y. Tang, P. Zhou et al., Cationic adsorption-induced microlevelling effect: a pathway to dendrite-free zinc anodes. Nano-Micro Lett. **17**(1), 202 (2025). https://doi.org/10.1007/s40820-025-01709-0
26. H. Yang, Y. Yang, W. Yang, G. Wu, R. Zhu, Correlating hydrogen evolution and zinc deposition/dissolution kinetics to the cyclability of metallic zinc electrodes. Energy Environ. Sci. **17**(5), 1975–1983 (2024). https://doi.org/10.1039/D3EE04515C
27. L. Qian, H. Zhu, T. Qin, R. Yao, J. Zhao et al., Ultralow-salt-concentration electrolyte for high-voltage aqueous Zn metal batteries. Adv. Funct. Mater. **33**(23), 2301118 (2023). https://doi.org/10.1002/adfm.202301118
28. A.G. Ilgen, E. Borguet, F.M. Geiger, J.M. Gibbs, V.H. Grassian et al., Bridging molecular-scale interfacial science with continuum-scale models. Nat. Commun. **15**(1), 5326 (2024). https://doi.org/10.1038/s41467-024-49598-y
29. B. Rehl, E. Ma, S. Parshotam, E.L. DeWalt-Kerian, T. Liu et al., Water structure in the electrical double layer and the contributions to the total interfacial potential at different surface charge densities. J. Am. Chem. Soc. **144**(36), 16338–16349 (2022). https://doi.org/10.1021/jacs.2c01830
30. Q. Wang, Z. Qu, D. Tian, Electric double layer theory of interfacial ionic liquids for capturing ion hierarchical aggregation and anisotropic dynamics. Adv. Energy Mater. **15**(13), 2402974 (2025). https://doi.org/10.1002/aenm.202402974
31. J. Luo, L. Xu, Y. Zhou, T. Yan, Y. Shao et al., Regulating the inner Helmholtz plane with a high donor additive for efficient anode reversibility in aqueous Zn-ion batteries. Angew. Chem. Int. Ed. **62**(21), e202302302 (2023). https://doi.org/10.1002/anie.202302302
32. Y. Yang, H. Hua, Z. Lv, M. Zhang, C. Liu et al., Reconstruction of electric double layer for long-life aqueous zinc metal batteries. Adv. Funct. Mater. **33**(10), 2212446 (2023). https://doi.org/10.1002/adfm.202212446
33. M. Zhang, H. Hua, P. Dai, Z. He, L. Han et al., Dynamically interfacial pH-buffering effect enabled by N-methylimidazole molecules as spontaneous proton pumps toward highly reversible zinc-metal anodes. Adv. Mater. **35**(15), e2208630 (2023). https://doi.org/10.1002/adma.202208630
34. Y. Zhu, G. Liang, X. Cui, X. Liu, H. Zhong et al., Engineering hosts for Zn anodes in aqueous Zn-ion batteries. Energy Environ. Sci. **17**(2), 369–385 (2024). https://doi.org/10.1039/d3ee03584k
35. C. Shuang, L. Zhen, Y. Xia, X. Wu, K. Wang et al., Step-edge guided homoepitaxy enables highly reversible Zn plating/stripping. Angew. Chem. Int. Ed. **64**(16), e202501176 (2025). https://doi.org/10.1002/anie.202501176
36. Z. Chen, J. Zhao, Q. He, M. Li, S. Feng et al., Texture control of commercial Zn foils prolongs their reversibility as aqueous battery anodes. ACS Energy Lett. **7**(10), 3564–3571 (2022). https://doi.org/10.1021/acsenergylett.2c01920
37. C. Yuan, L. Yin, P. Du, Y. Yu, K. Zhang et al., Microgroove-patterned Zn metal anode enables ultra-stable and low-overpotential Zn deposition for long-cycling aqueous batteries. Chem. Eng. J. **442**, 136231 (2022). https://doi.org/10.1016/j.cej.2022.136231
38. C. Yuan, J. Xiao, C. Liu, X. Zhan, Elucidating synergistic mechanisms of an anion–cation electrolyte additive for ultra-stable zinc metal anodes. J. Mater. Chem. A **12**(30), 19060–19068 (2024). https://doi.org/10.1039/D4TA03414G
39. J. Huang, Y. Zhong, H. Fu, Y. Zhao, S. Li et al., Interfacial biomacromolecular engineering toward stable ah-level aqueous zinc batteries. Adv. Mater. **36**(33), e2406257 (2024). https://doi.org/10.1002/adma.202406257
40. Y. Lv, M. Zhao, Y. Du, Y. Kang, Y. Xiao et al., Engineering a self-adaptive electric double layer on both electrodes for high-performance zinc metal batteries. Energy Environ. Sci. **15**(11), 4748–4760 (2022). https://doi.org/10.1039/D2EE02687B
41. Y. Zhao, D.G. Truhlar, The M06 suite of density functionals for main group thermochemistry, thermochemical kinetics, noncovalent interactions, excited states, and transition elements: two new functionals and systematic testing of four M06-class functionals and 12 other functionals. Theor. Chem. Acc. **120**(1), 215–241 (2008). https://doi.org/10.1007/s00214-007-0310-x
42. F. Weigend, R. Ahlrichs, Balanced basis sets of split valence, triple *zeta* valence and quadruple *zeta* valence quality for H to Rn: design and assessment of accuracy. Phys. Chem. Chem. Phys. **7**(18), 3297–3305 (2005). https://doi.org/10.1039/B508541A
43. A.V. Marenich, C.J. Cramer, D.G. Truhlar, Universal solvation model based on solute electron density and on a continuum model of the solvent defined by the bulk dielectric constant and atomic surface tensions. J. Phys. Chem. B **113**(18), 6378–6396 (2009). https://doi.org/10.1021/jp810292n
44. T. Lu, Q. Chen, Independent gradient model based on Hirshfeld partition: a new method for visual study of interactions in chemical systems. J. Comput. Chem. **43**(8), 539–555 (2022). https://doi.org/10.1002/jcc.26812
45. J. Zhang, T. Lu, Efficient evaluation of electrostatic potential with computerized optimized code. Phys. Chem. Chem. Phys. **23**(36), 20323–20328 (2021). https://doi.org/10.1039/d1cp02805g
46. T. Lu, F. Chen, Multiwfn: a multifunctional wavefunction analyzer. J. Comput. Chem. **33**(5), 580–592 (2012). https://doi.org/10.1002/jcc.22885
47. W. Sun, F. Wang, B. Zhang, M. Zhang, V. Küpers et al., A rechargeable zinc-air battery based on zinc peroxide chemistry. Science **371**(6524), 46–51 (2021). https://doi.org/10.1126/science.abb9554
48. B. Liu, C. Wei, Z. Zhu, Y. Fang, Z. Bian et al., Regulating surface reaction kinetics through ligand field effects for fast and reversible aqueous zinc batteries. Angew. Chem. Int. Ed.

61(44), e202212780 (2022). https://doi.org/10.1002/anie.202212780

49. M. Gutowski, J.H. Van Lenthe, J. Verbeek, F.B. Van Duijneveldt, G. Chałasinski, The basis set superposition error in correlated electronic structure calculations. Chem. Phys. Lett. **124**(4), 370–375 (1986). https://doi.org/10.1016/0009-2614(86)85036-9
50. G. Kresse, J. Furthmüller, Efficient iterative schemes for *ab initio* total-energy calculations using a plane-wave basis set. Phys. Rev. B **54**(16), 11169–11186 (1996). https://doi.org/10.1103/physrevb.54.11169
51. G. Kresse, J. Furthmüller, Efficiency of ab-initio total energy calculations for metals and semiconductors using a plane-wave basis set. Comput. Mater. Sci. **6**(1), 15–50 (1996). https://doi.org/10.1016/0927-0256(96)00008-0
52. J.P. Perdew, K. Burke, M. Ernzerhof, Generalized gradient approximation made simple. Phys. Rev. Lett. **77**(18), 3865–3868 (1996). https://doi.org/10.1103/physrevlett.77.3865
53. P.E. Blöchl, Projector augmented-wave method. Phys. Rev. B **50**(24), 17953–17979 (1994). https://doi.org/10.1103/physrevb.50.17953
54. S. Grimme, S. Ehrlich, L. Goerigk, Effect of the damping function in dispersion corrected density functional theory. J. Comput. Chem. **32**(7), 1456–1465 (2011). https://doi.org/10.1002/jcc.21759
55. M. Zhou, S. Guo, J. Li, X. Luo, Z. Liu et al., Surface-preferred crystal plane for a stable and reversible zinc anode. Adv. Mater. **33**(21), e2100187 (2021). https://doi.org/10.1002/adma.202100187
56. M.J. Abraham, T. Murtola, R. Schulz, S. Páll, J.C. Smith et al., GROMACS: High performance molecular simulations through multi-level parallelism from laptops to supercomputers. SoftwareX **1**, 19–25 (2015). https://doi.org/10.1016/j.softx.2015.06.001
57. S. Izadi, A.V. Onufriev, Accuracy limit of rigid 3-point water models. J. Chem. Phys. **145**(7), 074501 (2016). https://doi.org/10.1063/1.4960175
58. Z. Li, L.F. Song, P. Li, K.M. Merz Jr., Systematic parametrization of divalent metal ions for the OPC3, OPC, TIP3P-FB, and TIP4P-FB water models. J. Chem. Theory Comput. **16**(7), 4429–4442 (2020). https://doi.org/10.1021/acs.jctc.0c00194
59. J. Wang, R.M. Wolf, J.W. Caldwell, P.A. Kollman, D.A. Case, Development and testing of a general amber force field. J. Comput. Chem. **25**(9), 1157–1174 (2004). https://doi.org/10.1002/jcc.20035
60. M. Schauperl, P.S. Nerenberg, H. Jang, L.-P. Wang, C.I. Bayly et al., Non-bonded force field model with advanced restrained electrostatic potential charges (RESP2). Commun. Chem. **3**, 44 (2020). https://doi.org/10.1038/s42004-020-0291-4
61. G. Bussi, D. Donadio, M. Parrinello, Canonical sampling through velocity rescaling. J. Chem. Phys. **126**, 014101 (2007). https://doi.org/10.1063/1.2408420
62. H.J.C. Berendsen, J.P.M. Postma, W.F. van Gunsteren, A. DiNola, J.R. Haak, Molecular dynamics with coupling to an external bath. J. Chem. Phys. **81**(8), 3684–3690 (1984). https://doi.org/10.1063/1.448118
63. S. Nosé, A unified formulation of the constant temperature molecular dynamics methods. J. Chem. Phys. **81**(1), 511–519 (1984). https://doi.org/10.1063/1.447334
64. W.G. Hoover, Canonical dynamics: equilibrium phase-space distributions. Phys. Rev. A **31**(3), 1695–1697 (1985). https://doi.org/10.1103/physreva.31.1695
65. U. Essmann, L. Perera, M.L. Berkowitz, T. Darden, H. Lee et al., A smooth particle mesh Ewald method. J. Chem. Phys. **103**(19), 8577–8593 (1995). https://doi.org/10.1063/1.470117
66. D.M. York, T.A. Darden, L.G. Pedersen, The effect of long-range electrostatic interactions in simulations of macromolecular crystals: a comparison of the Ewald and truncated list methods. J. Chem. Phys. **99**(10), 8345–8348 (1993). https://doi.org/10.1063/1.465608
67. W. Humphrey, A. Dalke, K. Schulten, VMD: visual molecular dynamics. J. Mol. Graph. **14**(1), 33–38 (1996). https://doi.org/10.1016/0263-7855(96)00018-5
68. Q. Wu, M.T. McDowell, Y. Qi, Effect of the electric double layer (EDL) in multicomponent electrolyte reduction and solid electrolyte interphase (SEI) formation in lithium batteries. J. Am. Chem. Soc. **145**(4), 2473–2484 (2023). https://doi.org/10.1021/jacs.2c11807
69. L. Yu, N. Yao, Y.-C. Gao, Z.-H. Fu, B. Jiang et al., Probing the electric double layer structure at nitrogen-doped graphite electrodes by constant-potential molecular dynamics simulations. J. Energy Chem. **93**, 299–305 (2024). https://doi.org/10.1016/j.jechem.2024.01.058
70. Y. Wang, A. Kiziltas, P. Blanchard, T.R. Walsh, Calculation of 1D and 2D densities in VMD: a flexible and easy-to-use code. Comput. Phys. Commun. **266**, 108032 (2021). https://doi.org/10.1016/j.cpc.2021.108032
71. Z. Luo, Y. Xia, S. Chen, X. Wu, E. Akinlabi et al., A homogeneous plating/stripping mode with fine grains for highly reversible Zn anodes. Energy Environ. Sci. **17**(18), 6787–6798 (2024). https://doi.org/10.1039/D4EE02264E
72. S. Yang, A. Chen, Z. Tang, Z. Wu, P. Li et al., Regulating the electrochemical reduction kinetics by the steric hindrance effect for a robust Zn metal anode. Energy Environ. Sci. **17**(3), 1095–1106 (2024). https://doi.org/10.1039/D3EE02164E
73. H. Dou, X. Wu, M. Xu, R. Feng, Q. Ma et al., Steric-hindrance effect tuned ion solvation enabling high performance aqueous zinc ion batteries. Angew. Chem. Int. Ed. **63**(21), e202401974 (2024). https://doi.org/10.1002/anie.202401974
74. Q. Li, A. Chen, D. Wang, Z. Pei, C. Zhi, "Soft shorts" hidden in zinc metal anode research. Joule **6**(2), 273–279 (2022). https://doi.org/10.1016/j.joule.2021.12.009
75. H. Yang, D. Chen, R. Zhao, G. Li, H. Xu et al., Reunderstanding aqueous Zn electrochemistry from interfacial specific adsorption of solvation structures. Energy Environ. Sci. **16**(7), 2910–2923 (2023). https://doi.org/10.1039/D3EE00658A

© The authors

76. J. Dong, L. Su, H. Peng, D. Wang, H. Zong et al., Spontaneous molecule aggregation for nearly single-ion conducting sol electrolyte to advance aqueous zinc metal batteries: the case of tetraphenylporphyrin. Angew. Chem. Int. Ed. **63**(21), e202401441 (2024). https://doi.org/10.1002/anie.202401441
77. Y. Xia, Z. Hong, L. Zhou, S. Chen, Z. Luo et al., Multiscale simulations of surface adsorption characteristics of amino acids on zinc metal anode. J. Energy Chem. **87**, 153–161 (2023). https://doi.org/10.1016/j.jechem.2023.08.002
78. Z. Luo, Y. Xia, S. Chen, X. Wu, R. Zeng et al., Synergistic "anchor-capture" enabled by amino and carboxyl for constructing robust interface of Zn anode. Nano-Micro Lett. **15**(1), 205 (2023). https://doi.org/10.1007/s40820-023-01171-w
79. Q. Zong, Y. Yu, C. Liu, Q. Zhang, G. Wei et al., Decoupling "cling-cover-capture" triple effects on stable Zn anode/electrolyte interface. ACS Nano **18**(40), 27440–27450 (2024). https://doi.org/10.1021/acsnano.4c07803
80. Q. Zhao, W. Liu, X. Ni, H. Yu, C. Zhang et al., Steering interfacial renovation with highly electronegative Cl modulated trinity effect for exceptional durable zinc anode. Adv. Funct. Mater. **34**(41), 2404219 (2024). https://doi.org/10.1002/adfm.202404219
81. Q. He, G. Fang, Z. Chang, Y. Zhang, S. Zhou et al., Building ultra-stable and low-polarization composite Zn anode interface *via* hydrated polyzwitterionic electrolyte construction. Nano-Micro Lett. **14**(1), 93 (2022). https://doi.org/10.1007/s40820-022-00835-3
82. Q. Deng, S. You, W. Min, Y. Xu, W. Lin et al., Polymer molecules adsorption-induced zincophilic-hydrophobic protective layer enables highly stable Zn metal anodes. Adv. Mater. **36**(16), 2312924 (2024). https://doi.org/10.1002/adma.202312924
83. Y. Ding, L. Yin, T. Du, Y. Wang, Z. He et al., A trifunctional electrolyte enables aqueous zinc ion batteries with long cycling performance. Adv. Funct. Mater. **34**(30), 2314388 (2024). https://doi.org/10.1002/adfm.202314388
84. X. Wu, Y. Xia, S. Chen, Z. Luo, X. Zhang et al., Boosting the performance of aqueous zinc-ion battery by regulating the electrolyte solvation structure. EcoMat **6**(3), e12438 (2024). https://doi.org/10.1002/eom2.12438
85. K. Bao, M. Wang, Y. Zheng, P. Wang, L. Yang et al., Construction of low dielectric aqueous electrolyte with ethanol for highly stable Zn anode. Nano Energy **120**, 109089 (2024). https://doi.org/10.1016/j.nanoen.2023.109089
86. C. Huang, X. Zhao, S. Liu, Y. Hao, Q. Tang et al., Stabilizing zinc anodes by regulating the electrical double layer with saccharin anions. Adv. Mater. **33**(38), 2100445 (2021). https://doi.org/10.1002/adma.202100445
87. H. Zhang, F. Ning, Y. Guo, S. Subhan, X. Liu et al., Unraveling the mechanisms of aqueous zinc ion batteries *via* first-principles calculations. ACS Energy Lett. **9**(10), 4761–4784 (2024). https://doi.org/10.1021/acsenergylett.4c02014
88. L. Zeng, T. Wu, T. Ye, T. Mo, R. Qiao et al., Modeling galvanostatic charge-discharge of nanoporous supercapacitors. Nat. Comput. Sci. **1**(11), 725–731 (2021). https://doi.org/10.1038/s43588-021-00153-5
89. T. Yan, B. Wu, S. Liu, M. Tao, J. Liang et al., Sieving-type electric double layer with hydrogen bond interlocking to stable zinc metal anode. Angew. Chem. Int. Ed. **63**(47), e202411470 (2024). https://doi.org/10.1002/anie.202411470
90. X. Fang, C. Hu, X. Sun, H. Wang, J. Li, Robust hybrid solid electrolyte interface induced by Zn-poor electric double layer for a highly reversible zinc anode. Adv. Energy Mater. **14**(3), 2302499 (2024). https://doi.org/10.1002/aenm.202302499
91. Z. Hu, F. Zhang, F. Wu, H. Wang, A. Zhou et al., Screening metal cation additives driven by differential capacitance for Zn batteries. Energy Environ. Sci. **17**(13), 4794–4802 (2024). https://doi.org/10.1039/D4EE01127A
92. X. Yu, M. Chen, Z. Li, X. Tan, H. Zhang et al., Unlocking dynamic solvation chemistry and hydrogen evolution mechanism in aqueous zinc batteries. J. Am. Chem. Soc. **146**(25), 17103–17113 (2024). https://doi.org/10.1021/jacs.4c02558
93. H.K. Christenson, DLVO (Derjaguin–Landau–Verwey–Overbeek) theory and solvation forces between *mica* surfaces in polar and hydrogen-bonding liquids. J. Chem. Soc., Faraday Trans. 1 **80**(7), 1933 (1984). https://doi.org/10.1039/f19848001933
94. A.M. Smith, M. Borkovec, G. Trefalt, Forces between solid surfaces in aqueous electrolyte solutions. Adv. Colloid Interface Sci. **275**, 102078 (2020). https://doi.org/10.1016/j.cis.2019.102078
95. S.-Y. Lee, S.-H. Lee, J.-G. Park, Interaction forces between silica particles and wafer surfaces during chemical mechanical planarization of copper. J. Electrochem. Soc. **150**(5), G327 (2003). https://doi.org/10.1149/1.1566417
96. R. Zhao, H. Wang, H. Du, Y. Yang, Z. Gao et al., Lanthanum nitrate as aqueous electrolyte additive for favourable zinc metal electrodeposition. Nat. Commun. **13**(1), 3252 (2022). https://doi.org/10.1038/s41467-022-30939-8
97. Z. Tian, W. Guo, Z. Shi, Z. Alhubail, Y. Wang et al., The role of hydrogen bonding in aqueous batteries: correlating molecular-scale interactions with battery performance. ACS Energy Lett. **9**(10), 5179–5205 (2024). https://doi.org/10.1021/acsenergylett.4c02281
98. J. Luo, L. Xu, Y. Yang, S. Huang, Y. Zhou et al., Stable zinc anode solid electrolyte interphase *via* inner Helmholtz plane engineering. Nat. Commun. **15**(1), 6471 (2024). https://doi.org/10.1038/s41467-024-50890-0
99. L. Ma, T.P. Pollard, Y. Zhang, M.A. Schroeder, M.S. Ding et al., Functionalized phosphonium cations enable zinc metal reversibility in aqueous electrolytes. Angew. Chem. Int. Ed. **60**(22), 12438–12445 (2021). https://doi.org/10.1002/anie.202017020
100. K. Letchworth-Weaver, T.A. Arias, Joint density functional theory of the electrode-electrolyte interface: application to fixed electrode potentials, interfacial capacitances, and potentials of zero charge. Phys. Rev. B **86**(7), 075140 (2012). https://doi.org/10.1103/physrevb.86.075140
101. X. Wang, K. Liu, J. Wu, Demystifying the Stern layer at a metal-electrolyte interface: Local dielectric constant, specific ion adsorption, and partial charge transfer. J. Chem. Phys. **154**(12), 124701 (2021). https://doi.org/10.1063/5.0043963

102. R. Sundararaman, K. Letchworth-Weaver, K.A. Schwarz, D. Gunceler, Y. Ozhabes et al., JDFTx: software for joint density-functional theory. SoftwareX **6**, 278–284 (2017). https://doi.org/10.1016/j.softx.2017.10.006
103. J. Weng, W. Zhu, K. Yu, J. Luo, M. Chen et al., Enhancing Zn-metal anode stability: key effects of electrolyte additives on ion-shield-like electrical double layer and stable solid electrolyte interphase. Adv. Funct. Mater. **34**(18), 2314347 (2024). https://doi.org/10.1002/adfm.202314347
104. H. Yu, D. Chen, Q. Li, C. Yan, Z. Jiang et al., *In situ* construction of anode–molecule interface *via* lone-pair electrons in trace organic molecules additives to achieve stable zinc metal anodes. Adv. Energy Mater. **13**(22), 2300550 (2023). https://doi.org/10.1002/aenm.202300550
105. L. Wang, Y. Shao, Z. Fu, X. Zhang, J. Kang et al., Synergistically enhancing the selective adsorption for crystal planes to regulate the (002)-texture preferred Zn deposition *via* supramolecular host–guest units. Energy Environ. Sci. **18**(10), 4859–4871 (2025). https://doi.org/10.1039/d5ee00763a
106. S.-J. Zhang, J. Hao, D. Luo, P.-F. Zhang, B. Zhang et al., Dual-function electrolyte additive for highly reversible Zn anode. Adv. Energy Mater. **11**(37), 2102010 (2021). https://doi.org/10.1002/aenm.202102010
107. S. Chen, Y. Xia, R. Zeng, Z. Luo, X. Wu et al., Ordered planar plating/stripping enables deep cycling zinc metal batteries. Sci. Adv. **10**(10), eadn2265 (2024). https://doi.org/10.1126/sciadv.adn2265
108. R. Luo, X. Zheng, T. Jiang, D. Shen, M. Wang et al., Reshaping electrical double layer *via* synergistic dual additives for ah-level zinc battery. Adv. Energy Mater. (2025). https://doi.org/10.1002/aenm.202501658
109. M. Zhou, X. Luo, H. Li, S. Guo, Z. Tong et al., Interfacial Zn^{2+}-solvation regulator towards reversible and stable Zn anode. J. Energy Chem. **100**, 684–692 (2025). https://doi.org/10.1016/j.jechem.2024.08.061
110. J. Zhang, L.N.Y. Cao, R. Li, J. Yang, L. Li et al., Breaking mass transport limit for hydrogen evolution-inhibited and dendrite-free aqueous Zn batteries. Adv. Mater. **37**(1), e2410244 (2025). https://doi.org/10.1002/adma.202410244
111. F. Wan, L. Zhang, X. Dai, X. Wang, Z. Niu et al., Aqueous rechargeable zinc/sodium vanadate batteries with enhanced performance from simultaneous insertion of dual carriers. Nat. Commun. **9**(1), 1656 (2018). https://doi.org/10.1038/s41467-018-04060-8
112. X. Dou, X. Xie, S. Liang, G. Fang, Low-current-density stability of vanadium-based cathodes for aqueous zinc-ion batteries. Sci. Bull. **69**(6), 833–845 (2024). https://doi.org/10.1016/j.scib.2024.01.029

Publisher's Note Springer Nature remains neutral with regard to jurisdictional claims in published maps and institutional affiliations.

© The authors https://doi.org/10.1007/s40820-025-01915-w